Isolated ellipticals and their globular cluster systems

III. NGC 2271, NGC 2865, NGC 3962, NGC 4240 and IC 4889 [*]

R. Salinas[1, 2], A.Alabi[3, 4], T. Richtler[5], and R. R. Lane[5]

[1] Finnish Centre for Astronomy with ESO (FINCA), University of Turku, Väisäläntie 20, FI-21500 Piikkiö, Finland
[2] Department of Physics and Astronomy, Michigan State University, East Lansing, MI 48824, USA
[3] Tuorla Observatory, University of Turku, Väisäläntie 20, FI-21500 Piikkiö, Finland
[4] Centre for Astrophysics and Supercomputing, Swinburne University of Technology, Hawthorn, VIC 3122, Australia
[5] Departamento de Astronomía, Universidad de Concepción, Concepción, Chile

ABSTRACT

As tracers of star formation, galaxy assembly and mass distribution, globular clusters have provided important clues to our understanding of early-type galaxies. But their study has been mostly constrained to galaxy groups and clusters where early-type galaxies dominate, leaving the properties of the globular cluster systems (GCSs) of isolated ellipticals as a mostly uncharted territory. We present Gemini-South/GMOS $g'i'$ observations of five isolated elliptical galaxies: NGC 3962, NGC 2865, IC 4889, NGC 2271 and NGC 4240. Photometry of their GCSs reveals clear color bimodality in three of them, remaining inconclusive for the other two. All the studied GCSs are rather poor with a mean specific frequency $S_N \sim 1.5$, independently of the parent galaxy luminosity. Considering also previous work, it is clear that bimodality and especially the presence of a significant, even dominant, population of blue clusters occurs at even the most isolated systems, casting doubts on a possible accreted origin of metal-poor clusters as suggested by some models. Additionally, we discuss the possible existence of ultra-compact dwarfs around the isolated elliptical NGC 3962.

Key words. Galaxies: star clusters – Galaxies: individual: NGC 3962 – Galaxies: individual: NGC 2865 – Galaxies: individual: IC 4889 – Galaxies: individual: NGC 2271 – Galaxies: individual: NGC 4240

1. Introduction

The globular cluster systems (GCSs) of old, massive elliptical galaxies present an almost ubiquitous optical color bimodality (e.g. Kundu & Whitmore 2001; Larsen et al. 2001), thought as corresponding to a metallicity bimodality (e.g. Strader et al. 2007; Usher et al. 2012; Brodie et al. 2012), with caveats coming from possible non-linearities of the color-metallicity transformations introduced by horizontal-branch stars (Richtler 2006; Yoon et al. 2006; Chies-Santos et al. 2012; Blakeslee et al. 2012; Richtler 2013).

This "universal" bimodality has been obviously one of the main aspects the theories of GCS formation need to address. Many scenarios, not necessarily exclusive and somewhat overlapping, have been put forward over the years (e.g. Ashman & Zepf 1992; Forbes et al. 1997; Côté et al. 1998; Beasley et al. 2002; Rhode et al. 2005; Muratov & Gnedin 2010; Elmegreen et al. 2012; Tonini 2013).

Since elliptical galaxies are known to inhabit mostly high-density environments (e.g. Dressler 1980), most of the GCS studies, and hence the observational constraints to these theories,

have been naturally focused on galaxy clusters (e.g. Peng et al. 2006; Harris et al. 2006; Strader et al. 2006; Liu et al. 2011).

In the current reigning paradigm of galaxy formation, accretion and merging play the central roles (e.g. Cole et al. 1994; De Lucia et al. 2006), finding strong observational support (e.g. Ibata et al. 1994; Tal et al. 2009; van Dokkum et al. 2010). Simulations predict a different accretion history for elliptical galaxies in low-density environments compared to their high-density siblings (e.g. Niemi et al. 2010); but the impact that a low-density environment may have on the properties of a GCS has seldom been investigated (e.g Gebhardt & Kissler-Patig 1999), although it could give important evidence to discriminate between accretion driven (e.g. Côté et al. 1998; Hilker et al. 1999) and *in situ* (Forbes et al. 1997) scenarios.

Only a handful of isolated elliptical galaxies (IEs) have their GCS thoroughly studied (e.g. Spitler et al. 2008), given their paucity in the local environment. No field ellipticals are listed, for example, in the big compilation of Brodie & Strader (2006, see their Table 1), and only a handful can be seen in the newer compilation of Harris et al. (2013). Recently, Cho et al. (2012) studied 10 early-type galaxies in low density environments in the magnitude range $-18.5 < M_B < -20$ using HST/ACS, although solely using the Tully (1988) density parameter as isolation criterion.

This paper is part of an effort to understand the properties of GCS in IEs and their connections to their parent galaxies, collecting a large sample. This paper is a continuation of Lane et al. (2013, hereafter Paper I) who studied the GCS of the IE NGC 3585 and NGC 5812 using Washington photometry, and

Table 1. Basic data of the galaxies presented in this work.

Name	RA	Dec	l	b	Type	B_0^T (mag)	$(m-M)_0$ (mag)	M_B (mag)	fov (kpc)
NGC 2271	06:42:53.0	−23:28:34.0	233:13:30.5	−12:14:45.8	E/S0	12.10	32.51	−20.41	50.9
NGC 2865	09:23:30.2	−23:09:41.0	252:57:12.4	+18:56:29.9	E3	12.18	32.89	−20.71	60.5
NGC 3962	11:54:40.1	−13:58:30.0	282:39:10.7	+46:38:57.5	E1	11.59	32.74^a	−21.15	56.5
NGC 4240	12:17:24.3	−09:57:06.0	289:14:11.8	+52:00:46.3	E/cD?	14.01	32.07	−18.06	41.5
IC 4889	19:45:15.1	−54:20:39.0	343:32:15.1	−29:25:10.4	E5-6/S0	11.91	32.33	−20.42	46.8

Notes. Classification type comes from NED and HyperLeda databases, while total apparent *B* magnitudes are taken from RC3, except for NGC 4240, taken from HyperLeda. Distance moduli have been adopted from Tonry et al. (2001), except the one for NGC 4240 which comes from Reda et al. (2004). The last column gives the physical size covered by the GMOS FOV at each galaxy's distance.
[a] Considered as uncertain by Tonry et al. (2001).

Richtler et al. (2015, Paper II) who studied the IE NGC 7796. It is also complemented by the study of the field elliptical NGC 7507 (Caso et al. 2013) also conducted by our group.

1.1. The galaxy sample

As isolated galaxies give the opportunity to study galaxies without the interference of many of the processes that affect their structure and evolution in more crowded environments, many samples of IEs have been constructed, using diverse isolation criteria (Kuntschner et al. 2002; Smith et al. 2004; Stocke et al. 2004; Reda et al. 2004; Collobert et al. 2006; Nigoche-Netro et al. 2007; Fuse et al. 2012).

In this work we present observations of five IEs taken from the catalogues of Smith et al. (2004) and Reda et al. (2004); closer than ∼ 50 Mpc and observable from the southern hemisphere. The GCS of NGC 2865 and IC 4889 have been studied before, albeit with a smaller field of view (see below). In the following we give their main characteristics as found in the literature.

- **NGC 2271** is a E/S0 at a surface brightness fluctuation distance of 31.8 Mpc (Tonry et al. 2001) present in the catalogue of Reda et al. (2004). Reda et al. (2007) measured an age of 11.5±0.5 Gyr, with no evidence of radial age or metallicity gradients, while Hau & Forbes (2006) found strong rotation and kinematic signatures of an inner disk, which is also found on optical imaging (de Souza et al. 2004).
- **NGC 2865** is a E3 listed in the Reda et al. (2004) catalogue. It is known for the wealth of substructure (shells, tails, etc.) it possesses (Michard & Prugniel 2004; de Souza et al. 2004; Tal et al. 2009; Urrutia-Viscarra et al. 2014), being most probably a merger remnant (Hau et al. 1999), with a kinematically distinct core (Hau & Forbes 2006). It presents a remarkably steep age gradient from a central ∼ 1.5 Gyr (Sánchez-Blázquez et al. 2007; Reda et al. 2007) to ∼ 10 Gyr close to $1R_e$; exhibiting also a steep metallicity gradient (Reda et al. 2007). Its GCS was studied by Sikkema et al. (2006) using HST/ACS, finding a sizeable blue population consistent with a young/intermediate GC population (see also Trancho et al. 2014).
- **NGC 3962** is part of the Smith et al. (2004) sample of field ellipticals, with no companions as confirmed by Madore et al. (2004), and no signs of any tidal disturbance (Tal et al. 2009). Annibali et al. (2007) measured an age of 10 Gyr, while Serra & Oosterloo (2010) give an age of ∼2.5 Gyr.
- **NGC 4240** was taken from the Reda et al. (2004) catalogue. Reda et al. (2007) found a central age of 7.5 Gyr followed

Table 2. Observations log

Name	Obs. date (dd.mm.yyyy)	Exp. time (s) g'	i'	FWH M ('') g'	i'
NGC 2271	01.02.2012	9×419	9×315	0.73	0.74
NGC 2865	25.01.2012	6×480	6×340	0.63	0.50
	26.01.2012	6×490	6×350		
NGC 3962	22.02.2012	6×610	6×440	0.73	0.60
NGC 4240	02.02.2012	5×422	5×275	0.80	0.58
IC 4889	17.04.2012	3×575	5×355	–	0.75
	01.05.2012	3×575	1×355	0.49	–

Notes. The FWHM was measured on the combined images.

by a mild age gradient. The existence of an also shallow metallicity gradient is explained as indication of a past major merger. It possesses a kinematically distinct core and a mostly flat velocity dispersion profile (Hau & Forbes 2006).
- **IC 4889** is an E/S0 (Laurikainen et al. 2011) present in the Smith et al. (2004) catalogue, showing isophotal twisting (Tal et al. 2009) as well as a dusty disk (Smith et al. 2004). Serra & Oosterloo (2010) estimate an age of ∼ 3.6 Gyr. Its GCS has been studied by Gebhardt & Kissler-Patig (1999) using HST data, without finding evidence for bimodality.

The rest of the paper is distributed as follows: in Sect. 2.1 we describe the observations, as well as the data reduction and stellar photometry. In Sect. 3, we present the results on the color distribution of globular clusters, while radial profiles are presented in Sect. 4. GC luminosity functions are calculated in Sect. 5. Sect. 6 describes properties of the galaxies themselves and their connections to their GCS. Sect. 7 put the results into a broader context, before giving the conclusions in Sect. 8.

2. Observations and data reduction

2.1. Gemini-S/GMOS imaging

Imaging of the five galaxies was obtained using GMOS, mounted at the Gemini South Telescope, Cerro Pachón, Chile (program ID GS-2012A-Q-6). GMOS comprises three detectors covering in total a field-of-view of 5.5×5.5 arcmin^2, with a pixel scale of $0.146''$pixel^{-1} after a 2×2 binning. A set of dithered images in the SDSS filters g' and i' was obtained. Details of the observations can be seen in Table 2.

Image reduction was carried out inside the Gemini/IRAF[1] package (v 1.9). Reduction included bias subtraction, flat-

Table 3. Transformation equation coefficients for Eqs. 1 and 2 for the different galaxies.

Galaxy	Zero-point		Color term		N_{stars}	rms	
	g'	i'	g'	i'		g'	i'
NGC 2271	28.226 ± 0.005	27.900 ± 0.007	-0.052 ± 0.010	-0.024 ± 0.008	11	0.035	0.028
NGC 2865	28.253 ± 0.022	27.917 ± 0.012	-0.052 ± 0.010	-0.024 ± 0.008	15	0.046	0.041
NGC 3962	28.110 ± 0.034	27.770 ± 0.033	-0.052 ± 0.010	-0.024 ± 0.008	10	0.101	0.103
NGC 4240	28.240 ± 0.008	27.930 ± 0.007	-0.052 ± 0.010	-0.024 ± 0.008	33	0.023	0.021
IC 4889	28.209 ± 0.014	27.923 ± 0.009	-0.007 ± 0.014	0.001 ± 0.009	20	0.031	0.017

Notes. Extinction coefficients, taken from the Observatory webpages, are fixed for all equations with values $K_{g'} = 0.18$ and $K_{i'} = 0.08$. Color terms for NGC 2271, NGC 2865 and NGC 3962, were not fitted, but fixed; see main text for details. Additionally, the last four columns indicate parameters for Eq. 3 for both filters as described in Sect. 2.1.2.

fielding, detector mosaicing, fringe removal (for the i' exposures) and image co-addition. Processed bias, flat and fringe frames were retrieved from the Gemini Science Archive website. The FWHM measured on point sources in the final images can be seen in Table 2. Image quality in the IC 4889 exposures showed considerable variations between the two dates, for this reason the combined g' image takes data only from the May 2012 observations, while the combined i' was constructed with images coming from the night in April 2012 only.

2.1.1. Stellar photometry

In order to ease the source detection, images were first median filtered using a box of $10''$ aside. This process removes the parent galaxy light (everywhere but in the innermost arcseconds), leaving the point sources unaltered. A median value of the sky, determined from blank portions in the unsubtracted images distant from the central galaxy, was then added back to the images to keep the right photon statistics during the detection and photometry stages.

Object identification was carried out using SExtractor (Bertin & Arnouts 1996). The choice of the detection filter can have important consequences on the number of identified sources; while a Gaussian filter provides a better detection rate for the faintest sources, a "mexican hat" filter gives better results for sources very close to saturated stars or to the center of the galaxy unsubtracted residual. Given the relatively low Galactic latitude of some of the targets (NGC 2271 and NGC 2865) and the clumpy nature of some galaxy residuals (for example, IC 4889, see Sect. 6), the "mexican hat" filter is the most suitable option. SExtractor was then run twice on each image using both detection filters. Duplicate detections within 3 pixels were removed from the merged catalogues.

Concentric aperture and psf-fitting photometry was obtained using the stand-alone version of DAOPHOT/ALLSTAR (Stetson 1987) using as input the object coordinates from SExtractor. Between 30 and 50 bright isolated stars per field were chosen to determine the psf shape. Aperture corrections for each frame were measured using a subset of these stars.

Point sources were selected based on the behaviour of the SExtractor output parameter `class_star` and ALLSTAR parameter `sharp`. The accepted range of values for both parameters were determined from the results of the artificial stars experiments (see Sect. 2.1.2). Final cross-search between the stellar positions in the two different bands was done using DAOMATCH/DAOMASTER (Stetson 1993), keeping into the final catalogue only sources present in both bands with a tolerance of 3

Table 4. Completeness

Galaxy	α		m_{50}	
	g'	i'	g'	i'
NGC 2271	1.32	1.63	26.17	25.23
NGC 2865	1.90	2.95	27.32	26.24
NGC 3962	2.06	3.04	26.71	25.42
NGC 4240	2.41	4.24	26.45	25.77
IC 4889	3.29	2.25	26.82	24.41

pixels ($\sim 0.5''$) in their positions, thus weeding out remaining spurious detections.

Standard star frames from the southern extension of the Smith et al. (2002) catalogue observed on the same nights than our science frames were retrieved from the Gemini Science Archive. These frames were reduced following the same procedure of the science images, with the exception of the fringe correction, which was deemed to be unnecessary given the short exposures (~ 5 sec) in the i' filter. The number of standard stars measured for each night can be seen in Table 3. The transformation equations to the standard system used were

$$g'_{obs} = g'_{std} + Z_g + K_g(X - 1) + b_g(g' - i')_{std} \qquad (1)$$

$$i'_{obs} = i'_{std} + Z_i + K_i(X - 1) + b_i(g' - i')_{std} \qquad (2)$$

where X denotes the airmass of the observation. Coefficients were obtained using IRAF/PHOTCAL. The extinction coefficients were taken from the Gemini webpages and not fit, given the small range of airmasses covered by the observations. Also, when less than 20 stars were available on a field, the color terms were fixed to the values obtained for NGC 4240 for which the largest number of standard stars was available. Coefficients used for each galaxy can be seen in Table 3.

2.1.2. Photometry completeness

To study the level of completeness as a function of magnitude, artificial stars experiments were conducted using DAOPHOT/ADDSTAR. In each of the co-added frames (i.e. the ones where the galaxy light was not subtracted yet), we added 200 point sources covering a wide magnitude range. These new frames were then processed in the same way previously described: galaxy subtraction with median filtering, source detection with SExtractor and psf photometry with DAOPHOT. The procedure was repeated 50 times for a total of 10000 artificial stars per galaxy per filter. An example of the fraction of recovered stars as a function of magnitude can be seen in Fig. 1 (top panel).
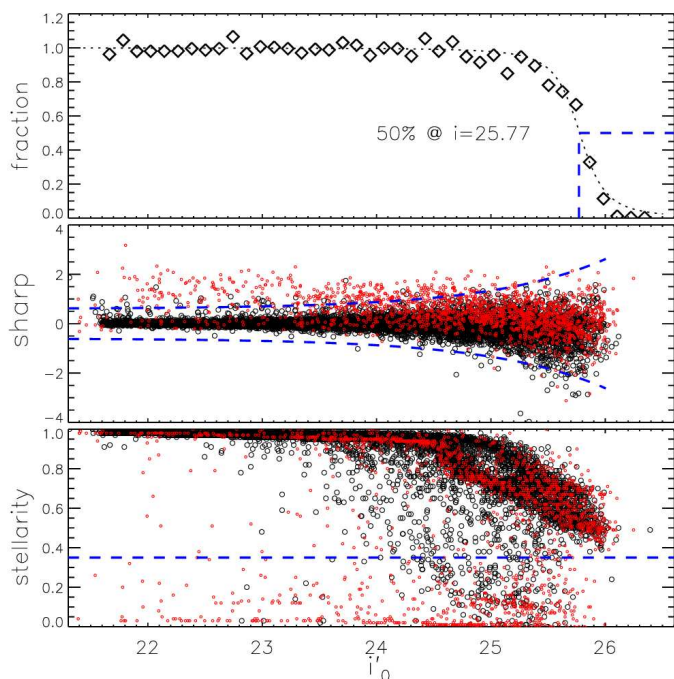
Fig. 1. *Top panel*: Fraction of recovered stars after the artificial stars experiment in the i' observations of NGC 4240. The dotted line is the fitted interpolation function (see Eq. 3). The dashed blue lines indicate the 50% level of completeness. *Middle panel*: Behaviour of the ALL-STAR parameter sharp. *Bottom panel*: SExtractor stellarity index. In both panels artificial stars are indicated with black circles, while the real sources are plotted in red. The blue dashed lines indicate the point source criteria applied to the science data based on the artificial one.

The fraction of recovered stars was fitted with the interpolation formula,

$$f = \frac{1}{2}\left(1 - \frac{\alpha(m - m_{50})}{\sqrt{1 + \alpha^2(m - m_{50})^2}}\right) \qquad (3)$$

which gives a good analytical description of the completeness, and have been used for many GC studies (e.g. McLaughlin et al. 1994; Fleming et al. 1995; Wehner et al. 2008; Alamo-Martínez et al. 2012). The free parameters α and m_{50} indicate the speed at which the detection rate falls at the faint level, and the 50% completeness, respectively. The values for both parameters for all fields and filters can be seen in Table 4.

Artificial stars experiments are not only useful to understand the detection limits, but also to understand the behaviour of the photometric measurements at these faint magnitudes. Separation between point and extended sources is a pervading problem in galactic and extragalactic studies and several methods are commonly used (e.g. Harris et al. 1991; Bertin & Arnouts 1996; Clem et al. 2008; Durret et al. 2009; Cho et al. 2012). In our case we preferred to use a combination of the SExtractor output parameter class_star, a stellarity likelihood, and the ALLSTAR parameter sharp, which measures deviations from the derived psf. In Fig. 1, we show an example of the behaviour of both parameters as a function of magnitude for the artificial stars (black circles) and the detected sources (red circles). Blue dashed lines show the limits that define the envelopes of the artificial stars. Only about 1%–2% of the total artificial stars lie beyond these limits. In the following we consider as point sources, the sources that satisfy these criteria.

2.1.3. Estimating the contamination

GCS of elliptical galaxies can have radial extensions up to hundreds of kpc (e.g. Richtler et al. 2011; Schuberth et al. 2012). Given the relatively small FOV provided by GMOS at the galaxies' distance (see column 10 in Table 1), a control field cannot be taken within the same telescope pointing as in wide-field studies (e.g. Rhode & Zepf 2001; Dirsch et al. 2003, Paper I), but has to be selected elsewhere. Control fields are necessary in order to determine the contamination the GC samples suffer; contamination coming partly from stars and from faint background galaxies that cannot be culled during the point-source selection (Sect. 2.1.1).

Since our observing program did not include any control field, an appropriate field was searched in the Gemini Science Archive, finding that the William Herschel Deep Field (WHDF) had similar total exposure times and image quality than our science data, and a very similar setup, using g' and i' filters on Gemini-N/GMOS (Gemini ID GN-2001B-SV-104, Metcalfe et al. 2001). The main caveat of using the WHDF as control field lies on its relatively high Galactic latitude ($b \sim -61°$), implying a likely underestimation of the stellar contamination, although at the faint levels where the bulk of the GC studied here are located, the dominant component of the contamination will be unresolved background galaxies, instead of stars (Faifer et al. 2011). The WHDF counts were hence complemented by adding star counts coming from the Besançon Galactic models (Robin et al. 2003) at each galaxies' position. As noted by Lane et al. (2011), comparisons between the Besançon models and pencil beams surveys can be problematic, due to stellar streams or other Local Group objects that are not included in the model. In our case, neither the WHDF nor the studied galaxies lie close to any of these features.

The reduction, photometry, artificial star experiments and point-source definition of the WHDF were carried out in the same way as the target galaxies, with the exception of the median filtering, in the absence of a dominant galaxy. The color-magnitude diagram of sources in the WHDF can be seen in Fig. 2 (bottom right panel). Since the completeness of the WHDF is shallower than the photometry in the NGC 2865 and NGC 4240 fields, the contamination in the faint end of these fields was estimated by multiplying the number of detected contaminant sources with the ratio of the interpolation functions (Eq. 3) of the galaxies to the one of the WHDF; generating bootstrapped samples with the expected number of contaminant sources.

2.2. SOAR/SAM imaging

Additional imaging of NGC 3962 was acquired on the night of April 22, 2014, using the SOAR Adaptive Module (SAM) and its Imager (SAMI) (Tokovinin et al. 2010, 2012). SAM is a ground layer adaptive optics system installed at the SOAR 4.1m telescope at Cerro Pachón, Chile. SAMI gives a field of view (FOV) of 3×3 arcmin with a scale of $0.091''\text{pixel}^{-1}$ (2×2 binning).

In total, 5×120, 3×120 and 5×120 seconds exposures were taken in the SDSS g, r and i filters, respectively. Details of the reduction process will be given in a forthcoming paper (Salinas et al. in prep), and only a preliminary calibration to the standard system, not crucial for its scientific goal, is given here. The FWHM measured on the combined images was $0.59''$, $0.55''$ and $0.50''$ in the g, r and i filters, respectively. This set of images, of higher resolution than the GMOS imaging, was used to study to the galaxy center where the deeper GMOS images were saturated. More details are given in Sect. 6.
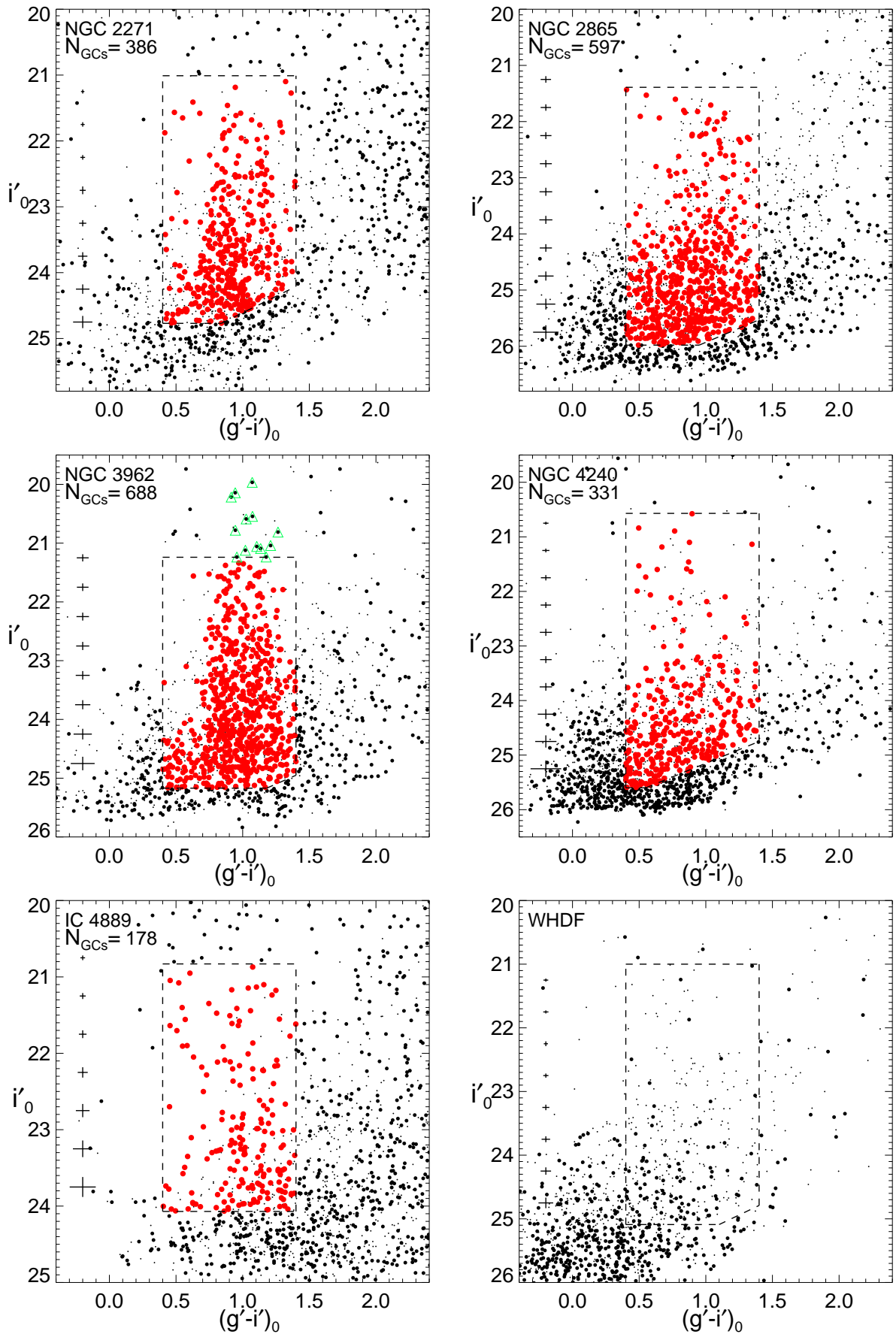
Fig. 2. Color-magnitude diagrams for sources detected around the five galaxies plus the control field (bottom right). Small black dots indicate the resolved sources, while the big black dots are the point sources as determined in Sect. 2.1.2. Globular clusters are depicted in red, inside the magnitude and color limits explained in the text. The number of GC candidates stated for each galaxy is *before* any decontamination and within the FOV. Green triangles in the NGC 3962 panel indicate UCD candidates (see Section 7.4).

3. The GC color distribution

Color-magnitude diagrams for all the point sources in our target galaxies can be seen in Fig. 2 as big black points, while resolved sources are depicted will small black dots. Globular cluster candidates were further limited to the color range $0.4 < (g - i)_0 < 1.4$, following previous GCS studies with the same filters (Forbes et al. 2004; Wehner et al. 2008; Faifer et al. 2011), but with a slightly bluer limit to allow the study of possible younger clusters (as in NGC 2685 Sikkema et al. 2006). The bright limit was fixed at $M_i = -11.5$ following Faifer et al. (2011), and the faint limit was given by the 80% completeness limit in both g and i. These bounding limits can be seen in Fig. 2 with dashed lines. Photometry was corrected for Galactic extinction using the Schlafly & Finkbeiner (2011) recalibration of Schlegel et al. (1998) dust maps.

The effect of the color-dependent completeness is negligible for NGC 3962 and the WHDF, mild for NGC 2771 and NGC 2865 and significant for NGC 4240. There is no color-dependent completeness for IC 4889.

None of the GCSs present an instantly obvious bimodal color distribution as their more massive counterparts in cluster environments (e.g. Dirsch et al. 2003), but NGC 3962 stands out by its healthy GCS. The GCSs with the deepest observations, NGC 4240 and NGC 2865, show a significant number of blue ($g' - i' \sim 0.5$) sources below $i' \sim 25$, which are likely compact background galaxies which have survived the point source determination process, while IC 4889 stands out by the presence of a significant blue population throughout the entire magnitude range ($21 \lesssim i \lesssim 24$), which seems absent in the rest of the galaxies (compare, for example, with NGC 3962).

Fig. 3 shows color histograms for the five GCSs, where the data has been binned using an optimum bin size, which depends on the sample size (Izenmann 1991). Each panel shows the raw (green dashed lines), background corrected (thick black lines) and background estimate (blue dotted lines) color histogram for each GCS. The background corrected histograms reveal that most of the GC candidates with colors $(g' - i')_0 \lesssim 0.7$ can be accounted as part of the contamination, except for NGC 2865 and especially NGC 4240 where a significant number of blue sources remain. The blue population in NGC 2865 is consistent with the results of Sikkema et al. (2006) who proposed the existence of a population of young clusters. Visually, the clearest case for bimodality can be seen in the IC 4889 color histogram, which contradicts the result of Gebhardt & Kissler-Patig (1999) which found no evidence of bimodality in the GCS of this galaxy.

In order to test the existence of bimodality in the GC color distributions more rigorously, we use a Gaussian mixture modeling (GMM) as implemented by Muratov & Gnedin (2010). GMM provides three indicators useful to discriminate between unimodal and bimodal distributions: the kurtosis of the distribution, k, which if negative indicates a flat-top distribution; the separation of the peaks, D, defined as $D = |\mu_{blue} - \mu_{red}|/[(\sigma_{blue}^2 + \sigma_{red}^2)/2]^{1/2}$, which, when larger than 2, indicates a clear separation between the peaks (Ashman et al. 1994); and a p–value, which gives the probability of obtaining the same χ^2 from a unimodal distribution. Uncertainties in each statistic are calculated with 100 bootstrapped realizations of the sample. To further test the robustness of the results, GMM was run 50 times on samples generated by randomly subtracting the number of contaminants expected per each color bin. The errors measured with this method are always within the errors obtained from the bootstrapped realizations (which are the quoted errors in Table 6), but additionally provide an uncertainty for the kurtosis which is not
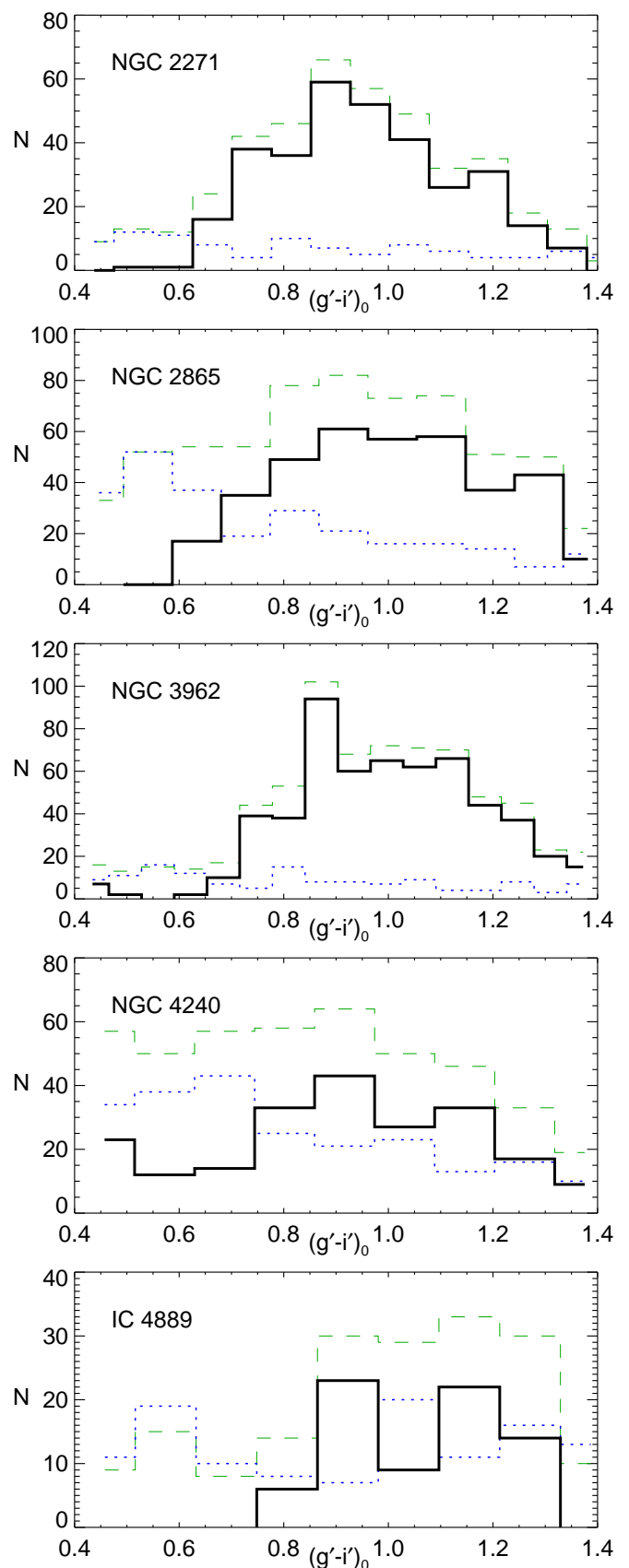
Fig. 3. Color histograms of the GCSs of the five target galaxies. The green dashed lines indicate the raw color distribution, the blue dotted line indicates the contamination in each field as determined in Sect. 2.1.3. The thick black lines show the background-corrected distributions.

Table 5. Globular cluster radial profiles.

Galaxy	power-law fit	
	σ_0	n
NGC 2271	1.69 ± 0.35	-2.18 ± 0.18
NGC 2865	1.38 ± 0.29	-1.88 ± 0.15
NGC 3962	1.29 ± 0.27	-1.81 ± 0.14
NGC 4240	-0.77 ± 0.30	-0.89 ± 0.15
IC 4889	-1.91 ± 0.84	-0.61 ± 0.43

given by GMM. Given the large number of blue sources in NGC 4240, GMM was run for sources with $0.6 \leq g - i \leq 1.4$, instead of $0.4 \leq g - i \leq 1.4$ as the rest of the galaxies.

The results of GMM applied over the background corrected GC samples can be seen in Table 6. Following Usher et al. (2012) we define a galaxy as showing clear bimodality when the conditions p-val< 0.1, $D > 2$ and $\kappa < 0$ are simultaneously met. These criteria are clearly fulfilled by NGC 2271, NGC 2865 and IC 4889. NGC 4240 also fulfill the criteria, although the large number of blue sources makes its case less reliable.

The most interesting case is given by NGC 3962. Despite being the galaxy in our sample with the richest GCS and with deep observations, its peak separation is barely larger than 2, the kurtosis is very close to zero and has the highest p-value, making the case for bimodality very doubtful. Intermediate-age globular clusters are known to smear out bimodality (e.g. Richtler et al. 2012), but the luminosity function shows no sign of intermediate-age clusters (see Sect. 5). Only observations using a longer wavelength baseline will provide a more definitive answer.

Additionally, Table 6 gives the red fraction, f_r, for each GCS. Red fractions, simply defined as the number of red clusters over the total number of clusters, are further discussed in Sect. 7.2.

4. The GC radial distribution

For photometry obtained with wide enough FOVs, the population of GCs detected around a galaxy is expected to drop off to a constant value at sufficiently extended radial positions from the galactic center. This constant number will represent foreground stars and faint background galaxies and the projected surface density of GCs as a function of galactocentric distance will give the radial distribution of GC candidates. In practice, given the rather limited FOV, we adopted the outermost bin of the radial distribution as background. Starting from the center of the images and considering only detected GC candidates brighter than the 80% completeness magnitude in the i filter, we grouped GC candidates and contaminants into concentric circular annuli, subtracted the contamination in each annulus and then divided by the effective area over which GC candidates are distributed.

We fitted power laws, $\sigma_{GC} = \sigma_0 r^n$, to the surface density profile of galaxies in our sample, where σ_{GC} is the number of GCs per square arc second and r is the projected radial distance. The fit was done for all GCSs in the fixed interval $40'' < r < 160''$ (horizontal dashed line in Fig. 4), which avoids the central zone of incompleteness produced by saturation, ill-subtracted galaxy and possible dusty features (see Sect. 6). Results of the fit can be seen as dotted blue lines in Fig. 4 and in Table 5.

The richest GCS, NGC3962, NGC 2271 and NGC 2865 follow a power law with index $n \sim -2$, as is the case for most giant ellipticals (e.g. Bassino et al. 2006). The galaxy which presents the larger deviation from the power law in the selected radial range is NGC 2865, which shows a small overabundance of GCs
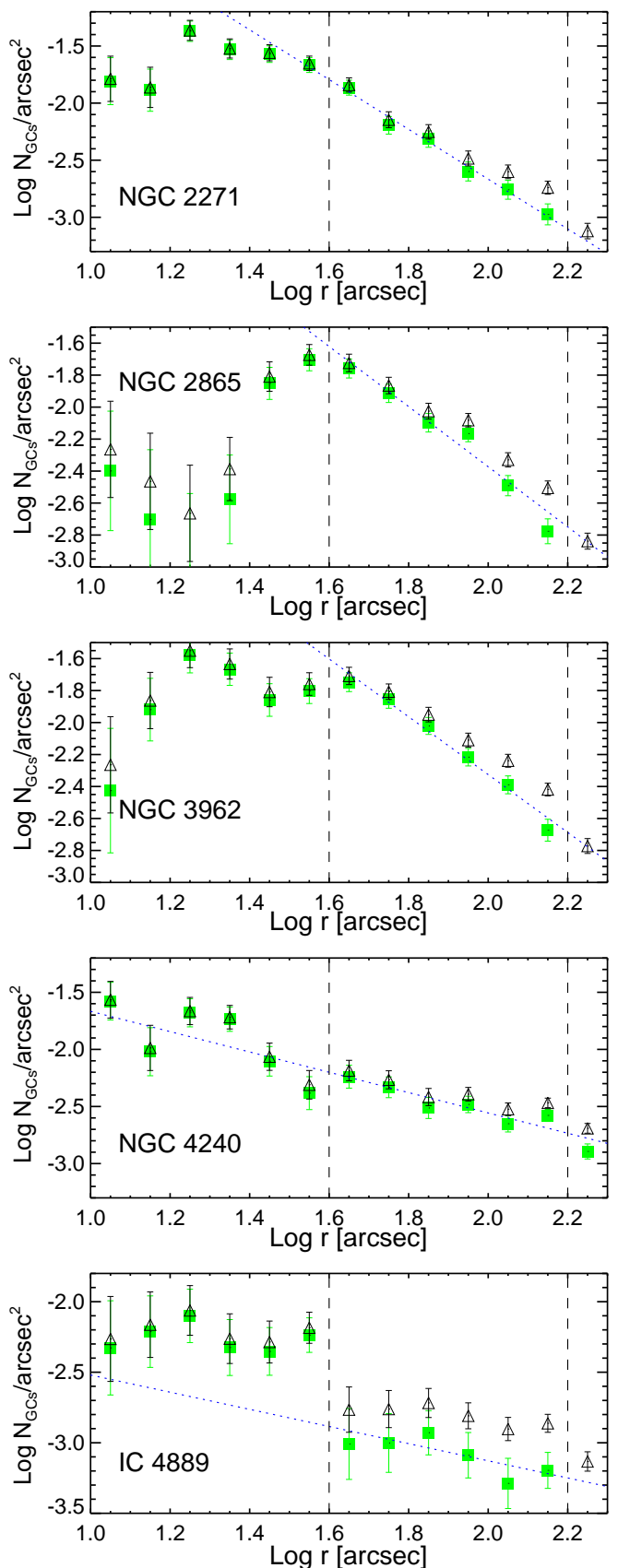

Fig. 4. The radial distribution of globular clusters in the studied galaxies. Open black triangles indicate the total population, while green filled squares depict the background subtracted population. Each distribution was fitted with a power law (blue dotted line), between the limits indicated by horizontal black dashed lines.

Table 6. GMM results.

Galaxy	N	μ_{blue}	μ_{red}	σ_{blue}	σ_{red}	f_r	D	κ	p-val
NGC 2271	295	0.896 ± 0.014	1.184 ± 0.025	0.125 ± 0.011	0.067 ± 0.011	0.17 ± 0.06	2.87 ± 0.26	-0.43 ± 0.04	0.001
NGC 2865	332	0.848 ± 0.043	1.125 ± 0.044	0.128 ± 0.019	0.096 ± 0.020	0.38 ± 0.14	2.43 ± 0.19	-0.87 ± 0.03	0.001
NGC 3962	557	0.947 ± 0.057	1.208 ± 0.041	0.156 ± 0.019	0.089 ± 0.019	0.19 ± 0.12	2.05 ± 0.37	-0.11 ± 0.04	0.007
NGC 4240	123	0.765 ± 0.055	1.098 ± 0.063	0.108 ± 0.033	0.103 ± 0.033	0.44 ± 0.17	3.08 ± 0.35	-1.16 ± 0.04	0.001
IC 4889	74	0.922 ± 0.015	1.187 ± 0.019	0.062 ± 0.010	0.081 ± 0.010	0.54 ± 0.07	3.65 ± 0.43	-1.25 ± 0.05	0.001

Notes. The second column indicates the number of (background subtracted) GC candidates used as input for GMM. Columns 3 and 4 indicate the peak color of the blue and red subpopulations, while columns 5 and 6 indicate the dispersion of the best fitting Gaussians. Column 7 indicates the red fraction, that is, the number of cluster associated with the red subpopulation divided by the total number of GC candidates. Column 8 is the peak separation as defined in Sect. 3, while column 9 is the sample kurtosis.

Table 7. GCLF fitted parameters and specific frequencies.

Galaxy	a_0	m_0	σ_m	N_{GC}	S_N	T_N	T_{blue}	T_{red}
NGC 2271	84 ± 1	24.54 (f)	1.16 ± 0.02	562 ± 9	1.46 ± 0.38	5.87 ± 0.10	4.87 ± 0.25	1.00 ± 0.35
NGC 2865	61 ± 2	24.92 (f)	1.02 ± 1.1	410 ± 8	1.00 ± 0.19	2.51 ± 0.05	1.55 ± 0.48	0.95 ± 0.35
NGC 3962	128 ± 15	24.50 ± 0.21	1.44 ± 0.15	854 ± 98	1.26 ± 0.57	2.87 ± 0.32	2.33 ± 0.39	0.55 ± 0.35
NGC 4240	–	–	–	84 ± 9	2.15 ± 0.80	2.53 ± 0.27	1.42 ± 0.55	1.11 ± 0.45
IC 4889	–	–	–	280 ± 17	0.85 ± 0.12	2.55 ± 0.15	1.17 ± 0.19	1.38 ± 0.20

at $\log r \sim 1.95$ (90′′) which might be associated with its intricate shell system.

NGC 4240 and IC 4889 present very shallow GC profiles, probably an effect of the low number of GCs present in these systems. Particularly problematic is the case of IC 4889 where an abrupt jump in the cluster distribution is visible at $r \sim 40''$. IC 4889 not only possesses a poor cluster system, but also is the galaxy with the shallowest observations of the set.

Finally, we note that the galaxies with fewer dusty features (NGC 2271 and NGC 4240, see Section 3) are the ones which follow closer the power law distribution inside the fit limit of 40′′.

5. Luminosity functions and distances

Luminosity functions in the i' band for the point sources in each galaxy field can be seen in Fig. 5 (blue dotted lines). Background/foreground contamination was estimated using the WHDF and Besançon models as in Sect. 2.1.3 (green dashes lines). The background-corrected luminosity functions, that is, the ones for the globular cluster candidates, are depicted with solid blue lines.

The inverted red arrows indicate the expected position of the turnover magnitud (TOM) of the globular cluster luminosity functions (GCLFs), assuming a universal value of $M_I^{\text{TOM}} = -8.46$ (Kundu & Whitmore 2001), transformed to M_i using Eq. 2 from Faifer et al. (2011), and distance moduli as given in Table 1.

For NGC 2271, NGC 2865 and NGC 3962, the contamination-subtracted GCLFs were modelled as the product of a Gaussian function with the completeness function (Eq. 3):

$$\frac{dN}{dm} = \frac{a_0}{\sqrt{2\pi}\sigma_m} \exp\left[\frac{(m-m_0)^2}{2\sigma_m^2}\right]^{\frac{1}{2}} \left[1 - \frac{\alpha(m-m_{50})}{\sqrt{1+\alpha^2(m-m_{50})^2}}\right],$$
(4)

where m_0 is the TOM and σ_m the width of the GCLF. The parameters for the completeness interpolation function are the ones derived in Sect. 2.1.2. The fitting of equation 4 was done using MPFIT, an implementation of non-linear square fitting in IDL (Markwardt 2009). The luminosity functions were fitted down

to the 50% completeness detection limit in i' (Table 4), with the exception of NGC 2865 were the fit was done using magnitudes down to the 80% limit, given the large number of sources at $i > 25.5$, which are probably faint background galaxies that escaped the point-source criteria defined in Sect. 2.1.

NGC 3962 is the only galaxy where the completeness limit is well beyond the TOM, therefore only for this galaxy we fit m_0, σ_m and the Gaussian amplitude, a_0. In the cases of NGC 2271 and NGC 2865, the TOM was fixed to its expected value based on its SBF distance (Tonry et al. 2001), and only σ_m and a_0 were fit. The results of the fit for these three galaxies can be seen in Table 7.

Only the case of NGC 3962 provides material to discuss its distance based on its GCLF. The distance modulus derived from the TOM position is 32.47 ± 0.20, while the Tonry et al. (2001) value, assumed throughout this paper, and based on SBF measurements is 32.74 ± 0.40. Even though they agree within the erros, the GCLF based distance is significantly lower than the SBF distance. If the SBF distance were the correct one, this would imply a slightly brighter TOM, $\text{TOM}_i = -8.24$, instead of the expected -7.97.

As discussed in Sect. 3, a possible explanation for the absence of a clear separation between the color peaks in NGC 3962 is the presence of an intermediate age population, but intermediate age populations have exactly the opposite effect, producing fainter TOMs (e.g. Richtler 2003), also even though metallicity is expected to have an influence on the TOM, this is minimized when using I band observations (e.g. Rejkuba 2012). A brighter TOM agrees with Blakeslee & Tonry (1996) who found evidence that the TOM varies with environment, with low-density galaxies having a brighter TOM (see also Villegas et al. 2010). A larger sample of IEs with deep enough observations would be necessary to confirm this.

The radial profiles in Fig. 4 indicate that the density of GCs quickly drops to values close to zero within the FOV, therefore, we did not attempt an extrapolation of the total number of clusters, N_{GC}, to obtain the fraction outside the FOV. The total number of GCs is then simply derived from the Gaussian fitted to the GCLF. In the cases where no fitting was attempted (NGC 4240 and IC4889), the total number of GCs was estimated by doubling the number of detected clusters above the TOM. The GCLF in NGC 4240 differs from the expected shape close to a
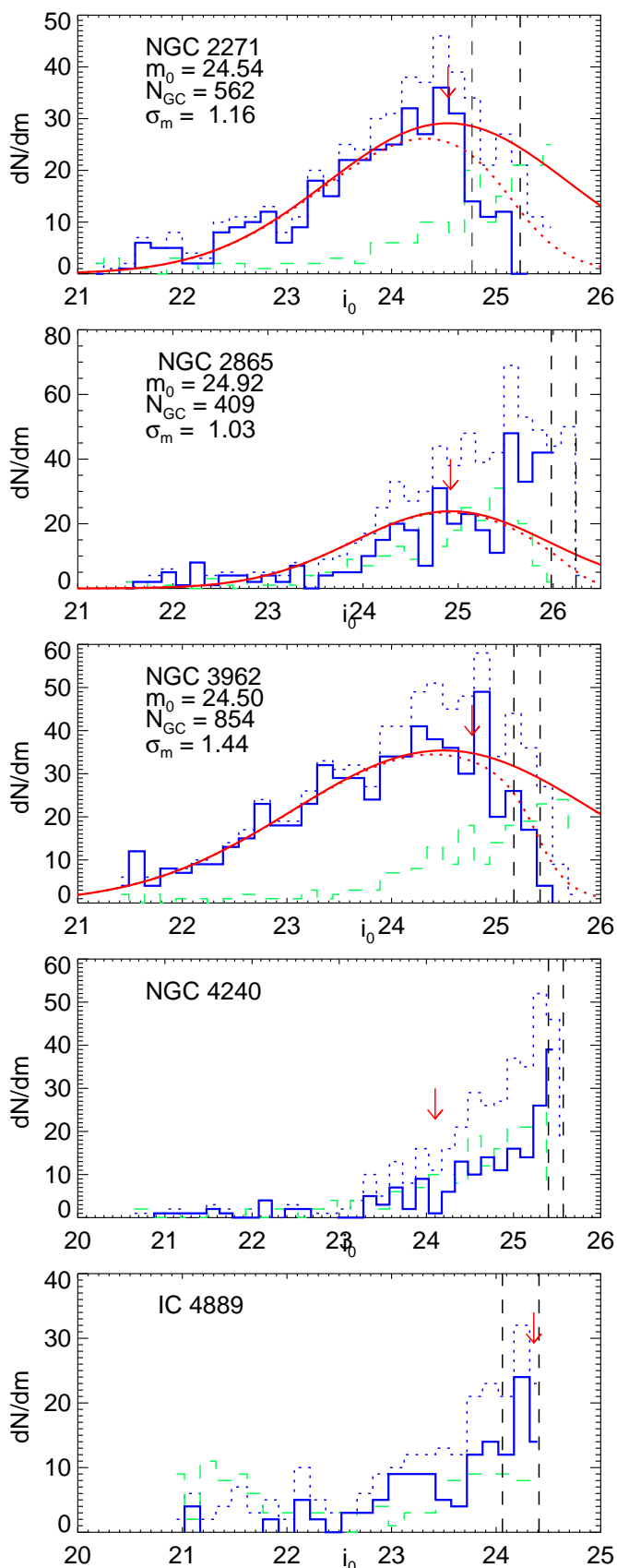
Fig. 5. GCLF for the five GCSs. Blue lines indicate the raw GCLF (dotted), the LF of the contamination (dashed), and the contamination-corrected GCLF (solid). Red lines indicate the fitted function (Eq. 4, dotted line) and its respective Gaussian. Vertical dashed black lines indicate the 80% and 50% completeness limits in i' as obtained in Sect. 2.1.2.

Gaussian, with a large number of very faint sources. Given the old age of the galaxy (Sect. 1.1) and the lack of evidence from the color maps of a recent meger event (Sect. 6), these are probably a residual contamination from background galaxies and not a faint young population of clusters. A similar GCLF is seen in NGC 3377 as shown by Cho et al. (2012).

Total number of GCs for the five galaxies can be seen in Table 7.

6. Galaxies surface brightness and colors

Surface brightness profiles of the galaxies were measured via ellipse fitting using the IRAF task ELLIPSE. All the other objects in each galaxy field were initially masked using the segmentation image produced by SExtractor, but additional regions (extended halos of bright stars, chip defects, etc) were interactively masked during the ELLIPSE execution. Once the regions to mask were established, ELLIPSE was run a second time, fixing the center of the ellipses as the mean central value of the ellipses with semi-major axes between 30 and 300 pixels. Sky brightness was calculated using the unmasked pixels outside the last measured isophote, taking the robust mean (Beers et al. 1990) of 40 random samples containing 800 sky pixels each. The uncertainty in the sky value was taken as the dispersion of these 40 sky measurements. Photometric calibration was done with the same equations as the point source photometry (Table 3), correcting for Galactic extinction following Schlafly & Finkbeiner (2011) dust maps.

The results from the ellipse fitting can be seen in Appendix B. The errors in the g' and i' surface brightness profiles comes from the sum in quadrature of the rms scatter in the intensity from the ellipse fitting and the uncertainty on the sky value. Surface brightness is given as function of the geometric mean radius, $r = a\sqrt{1 - \epsilon}$, where a is the fitted ellipse major axis and ϵ its ellipticity.

Color maps were also generated for each galaxy in order to look for color anomalies related to dust and possible past mergers.

NGC 2271 shows a flat color profile in the inner $\sim 30''$ along the major axis, with noticeable color gradient at larger radius (Fig. A.1). This is the normal behaviour for early-type galaxies (e.g. La Barbera et al. 2012), and compatible with the negligible age and metalicity gradients found by Reda et al. (2007) inside $0.5R_e$. No dusty features are visible.

Fig. A.2 (left panel), shows the color map of NGC 2865. NGC 2865 is widely considered as a merger remnant (Hau et al. 1999). The right panel shows the galaxy surface brightness map with the same scale. The large of number of shells, bluer than the galaxy body, have been discussed elsewhere (Malin & Carter 1983; Fort et al. 1986). We just emphasize a very narrow $\sim 20''$ long and $\sim 1.5''$ wide stream (white box in Fig. A.2), within the structure labeled "jet" in Fort et al. (1986) (their Fig. 3), pointing in projection directly to the galaxy center. Its blue color together with the large shell at the exact opposite side of the galaxy, probably makes it part of the same accretion process that produced the shells, although these very narrow radial features are not reproduced by simulations (e.g. Hernquist & Quinn 1987; Bílek et al. 2014), which show rather fan-like structures.

Fig. A.3 shows the $g - i$ color map for NGC 3962. The same structures detected by Buson et al. (1993) using Hα imaging can be seen. First, an extended, slightly off-centered arc-like structure about $15''$ from the galaxy center, with redder color than the underlying galaxy light. The SAM images (Fig. A.3, right

panel), also show a central elongated component, misaligned with the major and minor axis of the galaxy. Ionized gas is now commonly thought to be of external origin, especially for massive, round ellipticals (e.g. Sarzi et al. 2006), so even though the large scale structure of the galaxy does not reveal any evidence for past accretion, as indicated by the very low tidal parameter measured by Tal et al. (2009), the inner color structure might be indication of an older merger.

NGC 4240 shows a flatter color profile (Fig. A.4), similar to the one measured on the field elliptical NGC 7507 (Salinas et al. 2012). This agrees with the shallow age and metallicity gradients found by Reda et al. (2007). A notable feature is the $\Delta(g - i) \sim 0.15$ color difference, for the inner $\sim 15''$, between the South and North sections. Even though one would be tempted to relate it to the lop-sided rotation curve found by Hau & Forbes (2006) on the same scales, that rotation pattern was found roughly along the East-West axis. Another feature is a red plume of $\sim 15''$ in the SE direction (indicated with a black arrow in Fig.A.4). Both features were undetected by Reda et al. (2004).

IC 4889 shows a large spiral dusty feature (Fig. A.5), very similar to the one on NGC 3962. A remarkable feature is the unphysically red external halo. Despite our efforts to understand any issues with these images, we were unable to pinpoint the origin for the very flat i profile.

7. Discussion

7.1. The specific frequency of clusters in low- and high-density environments

The globular cluster specific frequency, S_N, defined by Harris & van den Bergh (1981) as

$$S_N = N_{GC} 10^{0.4(M_V+15)}, \tag{5}$$

connects the luminosity of a galaxy with its globular cluster population, in an attempt to measure how efficient is globular cluster formation compared to star formation. In Eq. 5, N_{GC} is the total number of globular clusters in a galaxy, and M_V is its absolute V magnitude.

We obtain S_N values for our sample using N_{GC} as obtained from the GCLF analysis in Section 5. Figure 6 (upper panel) contains a comparison between our results (red stars) with the Cho et al. (2012) sample of 10 low-density early-type galaxies (blue squares) and galaxies from the ACS Virgo Cluster Survey (ACSVCS, open black triangles, Peng et al. 2008). Additionally, we include the S_N of five more isolated/low-density ellipticals, NGC 3585, NGC 5812 (Lane et al. 2013), NGC 7507 (Caso et al. 2013), NGC 720 (Kartha et al. 2014) and NGC 7796 (Richtler et al. 2015) (green filled circles).

Fig. 6 (upper left panel) presents S_N as a function of stellar mass. Stellar masses for each galaxy in our sample and Cho et al. (2012) sample were derived using homogeneous K_s apparent magnitudes taken from the 2MASS Extended Source Catalog (Jarrett et al. 2003). K-band luminosities were transformed into stellar masses by using the Hubble type dependent mass-to-light ratios from Spitler et al. (2008), based on Bruzual & Charlot (2003) population models. Stellar masses for the ACSVCS galaxies were taken directly from Peng et al. (2008). Distances for the ACSVCS galaxies come from the recalibrated surface brightness fluctuations measurements given by Blakeslee et al. (2009).

Isolated ellipticals have a low S_N, scattered around $S_N \sim 1.5$, although there is a trend in the $10.5 < \log M_\star < 11.4$ in the sense that less massive galaxies have S_N closer to 2, while the more
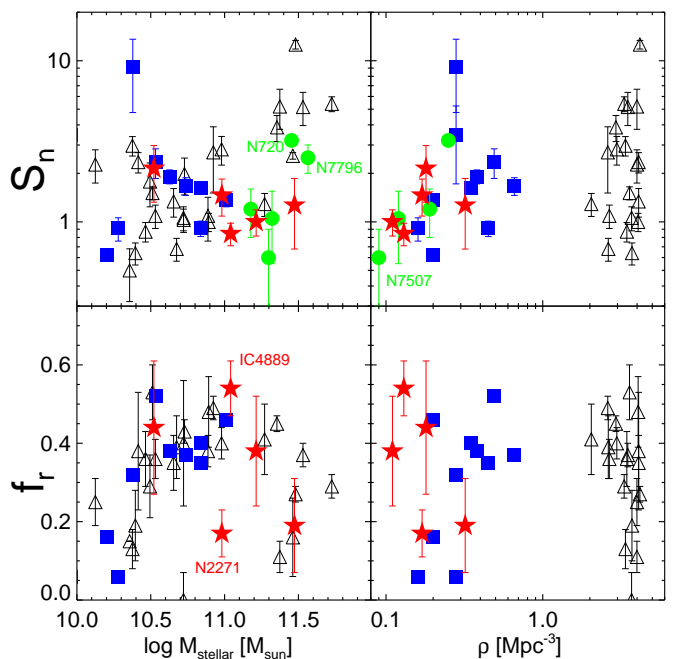
Fig. 6. Specific frequency (upper panels) and globular cluster red fraction (lower panels) as function of stellar mass and the Tully (1988) density parameter. Red symbols represent our sample, while blue squares are taken from the Cho et al. (2012) sample. Black open triangles are the results from the ACSVCS (Peng et al. 2008), while the the green filled circles are five more IEs described in the text.

massive are clustered around ~ 1. A Spearman's rank correlation test gives a coefficient of -0.74, with a two-sided significance of 0.002, indicating a high correlation. Considering a similar mass range, the opposite trend is seen for the Virgo GCSs (already discussed by Peng et al. 2008). IEs with $\log M_\star > 11.4$ show a diverse behavior, while NGC 3962 follows the trend of less massive galaxies, NGC 720 ($S_N = 3 \pm 0.2$, Kartha et al. 2014) and NGC 7796 ($S_N = 2.5 \pm 0.5$, Richtler et al. 2015) show an increased S_N, although still lower than Virgo ellipticals of similar mass.

The upper right panel of Fig. 6 shows now the S_N as a function of Tully (1988) density parameter. Galaxies in both low-density and high density environments share a broad range of S_N, but again a trend within the low-density sample can be seen, where the most isolated galaxies ($\rho \sim 0.1$) have even lower S_N, altough this trend almost totally driven by NGC 7507, the galaxy with the lowest density in the sample and with a surprisingly low S_N (Caso et al. 2013). Note that several galaxies in Virgo lack a density parameter, as well as NGC 4240 and NGC 7796, which are not included in the Tully (1988) catalog due to their distances.

The S_N depends on M_V, which in turns depends strongly on the age. Given that isolated ellipticals are considered late accretors, spanning a wide range of ages (e.g. Kuntschner et al. 2002; Reda et al. 2007), a true comparison with cluster ellipticals, believed to be homogeneously old, is hampered. To compare galaxies with possible different stellar populations, it is relevant to use the T_N parameter introduced by Zepf & Ashman (1993),

$$T_N = N_{GC}/(M_\star/10^9), \tag{6}$$

where the number of GCs is normalized to the stellar mass, $M_\star$, instead of M_V. Additionally, the parameters $T_{\rm blue}$ and $T_{\rm red}$ can
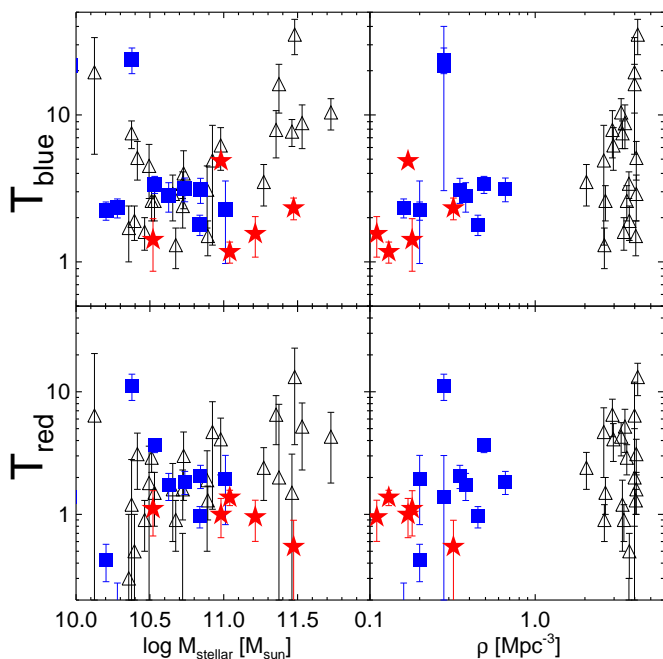
Fig. 7. T-parameters (see text) as function of stellar mass and density parameter. Symbols are the same as in Fig.6.

be defined, where the number of blue and red clusters are used instead of the total number, N_{GC}. The amount of blue and red clusters are obtained using the red fractions measured in Sect. 3.

Figure 7 shows $T_{\rm blue}$ and $T_{\rm red}$ for our sample together with the same galaxies used in the S_N comparison; the Cho et al. (2012) sample of low-density environment early-type galaxies, and early-type galaxies from the ACSVCS (Peng et al. 2006, 2008). Colors and symbols are the same as in Fig. 6.

The trend with mass seen for the S_N is not seen for $T_{\rm blue}$, although the more massive isolated ellipticals still show significantly lower values when compared to Virgo ellipticals of the same mass. The $T_{\rm red}$ values for our sample are systematically lower than the Cho et al. (2012) and ACSVCS samples in the range of masses described.

Finally, the right panels of Fig. 7 shows the behavior of the $T_{\rm red}$ and $T_{\rm blue}$ parameters as function of the density parameter. The trend seen for S_N among isolated and low-density galaxies is repeated for $T_{\rm blue}$ although less clearly. No clear trend is seen for $T_{\rm red}$, although if we solely considering our sample without the Cho et al. (2012) galaxies is clear than the $T_{\rm red}$ values for isolated ellitpicals span a narrow range close to 1 or less, while Virgo ellipticals have on average higher values.

7.2. The red fractions of isolated ellipticals

The proportion between blue and red clusters in a GCS is usually measured using the red fraction of GCs (e.g. Peng et al. 2006), that is, the fraction of red clusters compared to the entire population in a GCS. Red fractions are an important tool to discriminate between the possible scenarios of GCS formation.

Red fractions for our galaxies derived in Sect. 3 are presented in Fig. 6 (lower panels, red stars), together with red fractions for GCSs belonging to the ACSVCS (Peng et al. 2008, black triangles) and the 10 low-density ellipticals from (Cho et al. 2012, blue squares). Peng et al. (2008) red fractions are an updated version of the results presented by Peng et al. (2006), where red fractions were corrected for the radial incomplete-

ness that affects mostly the higher-luminosity ellipticals in their sample. Uncertainties have been taken from the original results of Peng et al. (2006) since updated values are not given by Peng et al. (2008). Uncertainties for the red fractions measured by Cho et al. (2012) are also not given in their paper.

The red fractions of Virgo galaxies present the same non-monotonic behavior seen in Peng et al. (2008, their Figure 8) as function of M_z instead of stellar mass. Red fractions increase from lower mass galaxies up to a maximum around $\log M_\star \sim 11$ beyond which red fractions experience a turnover. Interestingly, the somewhat lower red fractions for low-density ellipticals claimed by Cho et al. (2012) are not seen; in the $10 < \log M_\star < 11$ range the Cho et al. (2012) sample is indistinguishable from the Virgo galaxies. That we cannot see lower red fractions for the Cho et al. (2012) sample compared to the ACSVCS is probably based on, a) Cho et al. (2012) did not use the red fractions corrected by aperture given by Peng et al. (2008), instead using the uncorrected ones from Peng et al. (2006), and b) the comparison of red fractions was done as a function of M_B instead of stellar mass; for the same stellar mass, low-density ellipticals will appear brighter in the optical as they are on average younger than cluster ellipticals, so the claimed lower red fractions are only a population effect on the galaxies luminosities and not an intrinsic difference between the GCSs.

However, the galaxies presented in this paper appear to show systematic lower fractions than the Virgo galaxies at similar stellar mass, with the exception of IC4889. IC 4889 has the shallowest observations in our sample, thus the red fraction obtained for its GCS would appear to be uncertain, accounting for its unusually high value. It is important to note that, just like the values for the total number of GCs, the f_r are not corrected for unaccounted clusters outside the FOV, based on the quick decline of the GC density profiles (Sect. 4). If anything, wider field studies of these isolated galaxies will reveal even lower red fractions. We therefore conclude that red fractions in isolated ellipticals are equal or possibly lower than the values for high-density ellipticals.

Recently, Tonini (2013) introduced a model of GC formation based on hierarchical merging and the mass-metallicity relation for galaxies. An important feature of the model is the ability to make predictions for galaxies with rich and poor accretion histories, where poor-accretion galaxies end up with dominant red GC populations. If we associate galaxies with poor accretion histories to present day isolated ellipticals, our results are in strong disagreement with this model and in line with the results of Kartha et al. (2014) for lenticular galaxies. Additionally, it would be inconsistent with models proposing an accreted origin from dwarf galaxies for the blue population (e.g. Côté et al. 1998).

A strong argument against the accreted origin of blue clusters is the correlation between the peak color of the blue clusters and the luminosity of the parent galaxy (e.g. Larsen et al. 2001; Strader et al. 2004), which is not expected under an accretion scenario. Our finding of a dominant blue peak despite the likely absence of a rich accretion history, favours in-situ formation for GCs, where then the color bimodality would be rather explained by a non-linear color-metallicity relation in GCs (e.g. Yoon et al. 2006, 2011).

7.3. The color peaks

The mean color, or color peak, of the blue and red GC subpopulations have both been found to be functions of the parent galaxy luminosity (e.g. Larsen et al. 2001; Strader et al. 2004), which
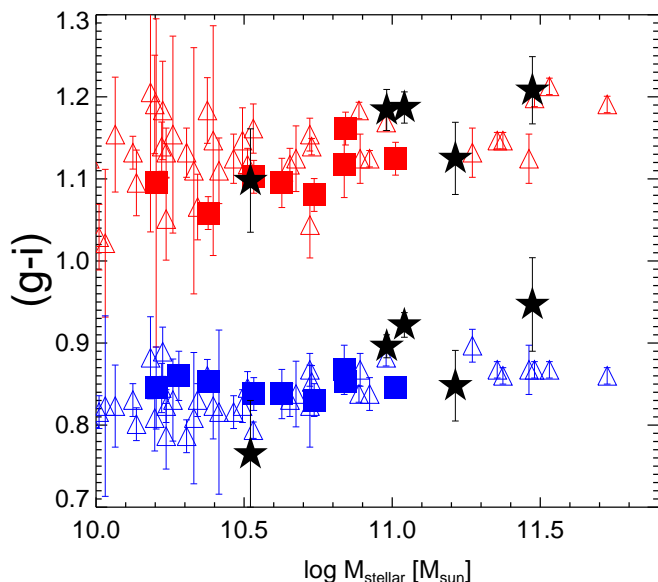
Fig. 8. Black stars indicate the red and blue peaks of the color distribution of GCs in our sample. Squares indicate galaxies from the Cho et al. (2012) sample, while open trinagles are the values from the ACSVCS (Peng et al. 2008).

suggest an intimate connection between galaxy and GC enrichment history.

In order to compare again with Cho et al. (2012) and Peng et al. (2008) samples, we transform $(g-z)$ colors from those studies into $(g-i)$ using the relation obtained by Usher et al. (2012) for 169 bonafide cluster in NGC 4365,

$$(g-i) = (0.735 \pm 0.009) \times (g-z) + (0.147 \pm 0.012)\, \text{mag.} \quad (7)$$

Fig. 8 shows that on average both peak magnitudes in our sample are redder, by a small but significant amount, than the Cho et al. (2012) and Peng et al. (2008) peak magnitudes. This is in contrast to the results of Cho et al. (2012) who found that the peak magnitudes for their GCS were slightly bluer compared to the Virgo galaxies from Peng et al. (2008), which also fits into the picture of isolated/field ellipticals having in average younger stellar populations. Given that our redder values go against this intuition, we believe our data may be affected by an error in its zeropoint photometry. We therefore restrict the analysis to an internal comparison between the galaxies in our sample.

Even though for the blue clusters, a slope may be more noticeable, this is dominated by the most massive (NGC 3962), and least massive galaxies (NGC 4240) of our sample, which are precisely the ones for which color bimodality is not totally supported (see Sect. 3). Moreover, the mass–peak color relation for blue clusters is expected to be even less pronounced for low-density environments (Strader et al. 2004). We conclude that no relation with galaxy mass is discernible for our sample, mostly limited by the narrow range of masses studied.

7.4. Ultra-compact dwarfs in NGC 3962?

The CMD of point sources around NGC 3962 shows a clear extension of the GC sequence above the selected brighter limit (Fig. 2, top left panel, green triangles). Seventeen point sources brighter than $i = 21.24$ ($M_i = -11.5$ at the galaxy's distance) and with $0.8 < (g-i)_0 < 1.4$ can be seen. In this same range of luminosity and colors only about three point sources are expected based on the comparison field (the WHDF, Fig. 2, bottom

right plot) and the Galactic model of Robin et al. (2003). Stellar systems of this bightness have been commonly labeled as "ultra-compact dwarfs" (UCDs, e.g. Drinkwater et al. 2000), due to the absence of counterparts in the Local Group.

Even though some of the low luminosity UCD candidates can be just bright GCs, given the uncertainty of 0.4 mag in the surface brightness distance modulus measured by Tonry et al. (2001), the correspondence between the expected and measured peak of the GCLF in NGC 3962 (Fig. 5) shows that the true distance cannot be too off, and hence most of these are genuinely brighter than the expected brightest GCs.

UCDs have been found mostly in galaxy groups and clusters (e.g. Mieske et al. 2008; Brodie et al. 2011), with formation channels mostly appealing to dynamical effects common in high-density environments (e.g. Hilker et al. 1999). If spectroscopically confirmed, the UCDs in NGC 3962 would be the first around an isolated elliptical, confirming that the formation of these objects is not restricted to high-density environments, following the finding of one UCD around the field spiral galaxy M 104 (Hau et al. 2009).

8. Summary and conclusions

In this paper we have studied the GCSs of five isolated elliptical galaxies, NGC 2271, NGC 2865, NGC 3962, NGC 4240 and IC 4889, using Gemini-S/GMOS gi imaging. Our main results are:

– The GMM analysis indicates clear bimodality for three out of 5 galaxies, while the two remaining show very short peak distances, making their bimodality less clear. In general, color bimodality is a common phenomenon down to the most isolated elliptical galaxies.
– The specific frequency of isolated ellipticals, S_N, is close to 1.5 irrespectibly of the galaxy mass. In the range $10.5 < \log M_\star < 11.4$ a small correlation can be seen, in the sense that more massive isolated ellpticals have smaller S_N, but for higher masses, larger S_N are measured.
– The conclusion of Cho et al. (2012) that galaxy mass is the main ruler of the properties of a GCS stems from the narrow range of masses used in their sample, biased towards low-luminosity galaxies. For galaxies with stellar masses $\log M_\star > 11$, environment, and not mass, has the highest impact determining some of the global properties (e.g. specific frequencies) of the GCSs.
– The red fractions show no significant difference with the ones seen in ellipticals in Virgo, making an accreted origin for the blue clusters doubtful. The slightly lower red fractions found by Cho et al. (2012) are a stellar population effect on the galaxies luminosities, and not intrinsic to the GCSs.

The last point assumes isolated ellipticals can be connected to poor accretion history galaxies found in cosmological simulations. Even though many isolated ellipticals show signs of *recent* mergers, to acquire knowledge of the entire accretion history, that is, to establish whether present day isolated ellipticals have been isolated throughout their lifetimes, is more difficult. As shown by Cooper et al. (2013), the outer surface brightness profiles of high-density and low-density galaxies should be remarkably different given their different accretion histories. The study of the outer surface brightness profiles of isolated ellipticals as proxy of their accretion histories will be the subject of forthcoming publications.

References

Alamo-Martínez, K. A., West, M. J., Blakeslee, J. P., et al. 2012, A&A, 546, A15
Annibali, F., Bressan, A., Rampazzo, R., Zeilinger, W. W., & Danese, L. 2007, A&A, 463, 455
Ashman, K. M., Bird, C. M., & Zepf, S. E. 1994, AJ, 108, 2348
Ashman, K. M. & Zepf, S. E. 1992, ApJ, 384, 50
Bassino, L. P., Faifer, F. R., Forte, J. C., et al. 2006, A&A, 451, 789
Beasley, M. A., Baugh, C. M., Forbes, D. A., Sharples, R. M., & Frenk, C. S. 2002, MNRAS, 333, 383
Beers, T. C., Flynn, K., & Gebhardt, K. 1990, AJ, 100, 32
Bertin, E. & Arnouts, S. 1996, A&AS, 117, 393
Bílek, M., Ebrová, I., Jungwiert, B., Jílková, L., & Bartošková, K. 2014, ArXiv e-prints
Blakeslee, J. P., Cho, H., Peng, E. W., et al. 2012, ApJ, 746, 88
Blakeslee, J. P., Jordán, A., Mei, S., et al. 2009, ApJ, 694, 556
Blakeslee, J. P. & Tonry, J. L. 1996, ApJ, 465, L19
Brodie, J. P., Romanowsky, A. J., Strader, J., & Forbes, D. A. 2011, AJ, 142, 199
Brodie, J. P. & Strader, J. 2006, ARA&A, 44, 193
Brodie, J. P., Usher, C., Conroy, C., et al. 2012, ApJ, 759, L33
Bruzual, G. & Charlot, S. 2003, MNRAS, 344, 1000
Buson, L. M., Sadler, E. M., Zeilinger, W. W., et al. 1993, A&A, 280, 409
Caso, J. P., Richtler, T., Bassino, L. P., et al. 2013, A&A, 555, A56
Chies-Santos, A. L., Larsen, S. S., Cantiello, M., et al. 2012, A&A, 539, A54
Cho, J., Sharples, R. M., Blakeslee, J. P., et al. 2012, MNRAS, 422, 3591
Clem, J. L., Vanden Berg, D. A., & Stetson, P. B. 2008, AJ, 135, 682
Cole, S., Aragon-Salamanca, A., Frenk, C. S., Navarro, J. F., & Zepf, S. E. 1994, MNRAS, 271, 781
Collobert, M., Sarzi, M., Davies, R. L., Kuntschner, H., & Colless, M. 2006, MNRAS, 370, 1213
Cooper, A. P., D'Souza, R., Kauffmann, G., et al. 2013, MNRAS, 434, 3348
Côté, P., Marzke, R. O., & West, M. J. 1998, ApJ, 501, 554
De Lucia, G., Springel, V., White, S. D. M., Croton, D., & Kauffmann, G. 2006, MNRAS, 366, 499
de Souza, R. E., Gadotti, D. A., & dos Anjos, S. 2004, ApJS, 153, 411
Dirsch, B., Richtler, T., Geisler, D., et al. 2003, AJ, 125, 1908
Dressler, A. 1980, ApJ, 236, 351
Drinkwater, M. J., Jones, J. B., Gregg, M. D., & Phillipps, S. 2000, PASA, 17, 227
Durret, F., Slezak, E., & Adami, C. 2009, A&A, 506, 637
Elmegreen, B. G., Malhotra, S., & Rhoads, J. 2012, ApJ, 757, 9
Faifer, F. R., Forte, J. C., Norris, M. A., et al. 2011, MNRAS, 416, 155
Fleming, D. E. B., Harris, W. E., Pritchet, C. J., & Hanes, D. A. 1995, AJ, 109, 1044
Forbes, D. A., Brodie, J. P., & Grillmair, C. J. 1997, AJ, 113, 1652
Forbes, D. A., Faifer, F. R., Forte, J. C., et al. 2004, MNRAS, 355, 608
Fort, B. P., Prieur, J.-L., Carter, D., Meatheringham, S. J., & Vigroux, L. 1986, ApJ, 306, 110
Fuse, C., Marcum, P., & Fanelli, M. 2012, AJ, 144, 57
Gebhardt, K. & Kissler-Patig, M. 1999, AJ, 118, 1526
Harris, W. E., Allwright, J. W. B., Pritchet, C. J., & van den Bergh, S. 1991, ApJS, 76, 115
Harris, W. E., Harris, G. L. H., & Alessi, M. 2013, ApJ, 772, 82
Harris, W. E. & van den Bergh, S. 1981, AJ, 86, 1627
Harris, W. E., Whitmore, B. C., Karakla, D., et al. 2006, ApJ, 636, 90
Hau, G. K. T., Carter, D., & Balcells, M. 1999, MNRAS, 306, 437
Hau, G. K. T. & Forbes, D. A. 2006, MNRAS, 371, 633
Hau, G. K. T., Spitler, L. R., Forbes, D. A., et al. 2009, MNRAS, 394, L97
Hernquist, L. & Quinn, P. J. 1987, ApJ, 312, 1
Hilker, M., Infante, L., & Richtler, T. 1999, A&AS, 138, 55
Ibata, R. A., Gilmore, G., & Irwin, M. J. 1994, Nature, 370, 194
Izenmann, A. J. 1991, Am. Stat. Assoc., 86, 205
Jarrett, T. H., Chester, T., Cutri, R., Schneider, S. E., & Huchra, J. P. 2003, AJ, 125, 525
Kartha, S. S., Forbes, D. A., Spitler, L. R., et al. 2014, MNRAS, 437, 273
Kundu, A. & Whitmore, B. C. 2001, AJ, 121, 2950

Kuntschner, H., Smith, R. J., Colless, M., et al. 2002, MNRAS, 337, 172
La Barbera, F., Ferreras, I., de Carvalho, R. R., et al. 2012, MNRAS, 426, 2300
Lane, R. R., Kiss, L. L., Lewis, G. F., et al. 2011, A&A, 530, A31
Lane, R. R., Salinas, R., & Richtler, T. 2013, A&A, 549, A148
Larsen, S. S., Brodie, J. P., Huchra, J. P., Forbes, D. A., & Grillmair, C. J. 2001, AJ, 121, 2974
Laurikainen, E., Salo, H., Buta, R., & Knapen, J. H. 2011, MNRAS, 418, 1452
Liu, C., Peng, E. W., Jordán, A., et al. 2011, ApJ, 728, 116
Madore, B. F., Freedman, W. L., & Bothun, G. D. 2004, ApJ, 607, 810
Malin, D. F. & Carter, D. 1983, ApJ, 274, 534
Markwardt, C. B. 2009, in Astronomical Society of the Pacific Conference Series, Vol. 411, Astronomical Data Analysis Software and Systems XVIII, ed. D. A. Bohlender, D. Durand, & P. Dowler, 251
McLaughlin, D. E., Harris, W. E., & Hanes, D. A. 1994, ApJ, 422, 486
Metcalfe, N., Shanks, T., Campos, A., McCracken, H. J., & Fong, R. 2001, MNRAS, 323, 795
Michard, R. & Prugniel, P. 2004, A&A, 423, 833
Mieske, S., Hilker, M., Jordán, A., et al. 2008, A&A, 487, 921
Muratov, A. L. & Gnedin, O. Y. 2010, ApJ, 718, 1266
Niemi, S., Heinämäki, P., Nurmi, P., & Saar, E. 2010, MNRAS, 471
Nigoche-Netro, A., Moles, M., Ruelas-Mayorga, A., Franco-Balderas, A., & Kjørgaard, P. 2007, A&A, 472, 773
Peng, E. W., Jordán, A., Côté, P., et al. 2006, ApJ, 639, 95
Peng, E. W., Jordán, A., Côté, P., et al. 2008, ApJ, 681, 197
Reda, F. M., Forbes, D. A., Beasley, M. A., O'Sullivan, E. J., & Goudfrooij, P. 2004, MNRAS, 354, 851
Reda, F. M., Proctor, R. N., Forbes, D. A., Hau, G. K. T., & Larsen, S. S. 2007, MNRAS, 377, 1772
Rejkuba, M. 2012, Ap&SS, 341, 195
Rhode, K. L. & Zepf, S. E. 2001, AJ, 121, 210
Rhode, K. L., Zepf, S. E., & Santos, M. R. 2005, ApJ, 630, L21
Richtler, T. 2003, in Lecture Notes in Physics, Berlin Springer Verlag, Vol. 635, Stellar Candles for the Extragalactic Distance Scale, ed. D. Alloin & W. Gieren, 281–305
Richtler, T. 2006, Bulletin of the Astronomical Society of India, 34, 83
Richtler, T. 2013, in Astronomical Society of the Pacific Conference Series, Vol. 470, 370 Years of Astronomy in Utrecht, ed. G. Pugliese, A. de Koter, & M. Wijburg, 327
Richtler, T., Bassino, L. P., Dirsch, B., & Kumar, B. 2012, A&A, 543, A131
Richtler, T., Salinas, R., Lane, R. R., Hilker, M., & Schirmer, M. 2015, A&A, 574, A21
Richtler, T., Salinas, R., Misgeld, I., et al. 2011, A&A, 531, A119
Robin, A. C., Reylé, C., Derrière, S., & Picaud, S. 2003, A&A, 409, 523
Salinas, R., Richtler, T., Bassino, L. P., Romanowsky, A. J., & Schuberth, Y. 2012, A&A, 538, A87
Sánchez-Blázquez, P., Forbes, D. A., Strader, J., Brodie, J., & Proctor, R. 2007, MNRAS, 377, 759
Sarzi, M., Falcón-Barroso, J., Davies, R. L., et al. 2006, MNRAS, 366, 1151
Schlafly, E. F. & Finkbeiner, D. P. 2011, ApJ, 737, 103
Schlegel, D. J., Finkbeiner, D. P., & Davis, M. 1998, ApJ, 500, 525
Schuberth, Y., Richtler, T., Hilker, M., et al. 2012, A&A, 544, A115
Serra, P. & Oosterloo, T. A. 2010, MNRAS, 401, L29
Sikkema, G., Peletier, R. F., Carter, D., Valentijn, E. A., & Balcells, M. 2006, A&A, 458, 53
Smith, J. A., Tucker, D. L., Kent, S., et al. 2002, AJ, 123, 2121
Smith, R. M., Martínez, V. J., & Graham, M. J. 2004, ApJ, 617, 1017
Spitler, L. R., Forbes, D. A., Strader, J., Brodie, J. P., & Gallagher, J. S. 2008, MNRAS, 385, 361
Stetson, P. B. 1987, PASP, 99, 191
Stetson, P. B. 1993, in IAU Colloq. 136: Stellar Photometry - Current Techniques and Future Developments, ed. C. J. Butler & I. Elliott, 291
Stocke, J. T., Keeney, B. A., Lewis, A. D., Epps, H. W., & Schild, R. E. 2004, AJ, 127, 1336
Strader, J., Beasley, M. A., & Brodie, J. P. 2007, AJ, 133, 2015
Strader, J., Brodie, J. P., & Forbes, D. A. 2004, AJ, 127, 3431
Strader, J., Brodie, J. P., Spitler, L., & Beasley, M. A. 2006, AJ, 132, 2333
Tal, T., van Dokkum, P. G., Nelan, J., & Bezanson, R. 2009, AJ, 138, 1417
Tokovinin, A., Cantarutti, R., Tighe, R., et al. 2010, PASP, 122, 1483
Tokovinin, A., Tighe, R., Schurter, P., et al. 2012, in Society of Photo-Optical Instrumentation Engineers (SPIE) Conferenc e Series, Vol. 8447, Society of Photo-Optical Instrumentation Engineers (SPIE) Conferenc e Series
Tonini, C. 2013, ApJ, 762, 39
Tonry, J. L., Dressler, A., Blakeslee, J. P., et al. 2001, ApJ, 546, 681
Trancho, G., Miller, B. W., Schweizer, F., Burdett, D. P., & Palamara, D. 2014, ApJ, 790, 122
Tully, R. B. 1988, Nearby galaxies catalog
Urrutia-Viscarra, F., Arnaboldi, M., Mendes de Oliveira, C., et al. 2014, A&A, 569, A97
Usher, C., Forbes, D. A., Brodie, J. P., et al. 2012, MNRAS, 426, 1475
van Dokkum, P. G., Whitaker, K. E., Brammer, G., et al. 2010, ApJ, 709, 1018
Villegas, D., Jordán, A., Peng, E. W., et al. 2010, ApJ, 717, 603
Wehner, E. M. H., Harris, W. E., Whitmore, B. C., Rothberg, B., & Woodley, K. A. 2008, ApJ, 681, 1233
Yoon, S.-J., Lee, S.-Y., Blakeslee, J. P., et al. 2011, ApJ, 743, 150
Yoon, S.-J., Yi, S. K., & Lee, Y.-W. 2006, Science, 311, 1129
Zepf, S. E. & Ashman, K. M. 1993, MNRAS, 264, 611
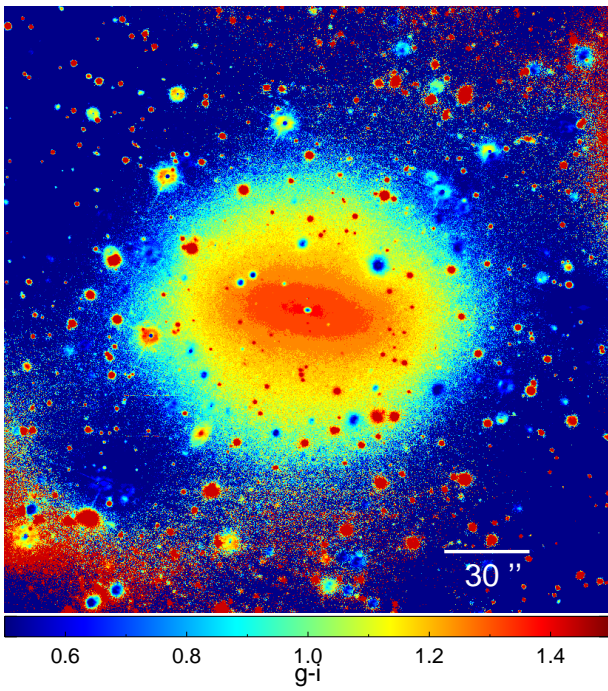
Fig. A.1. NGC 2271 color map.
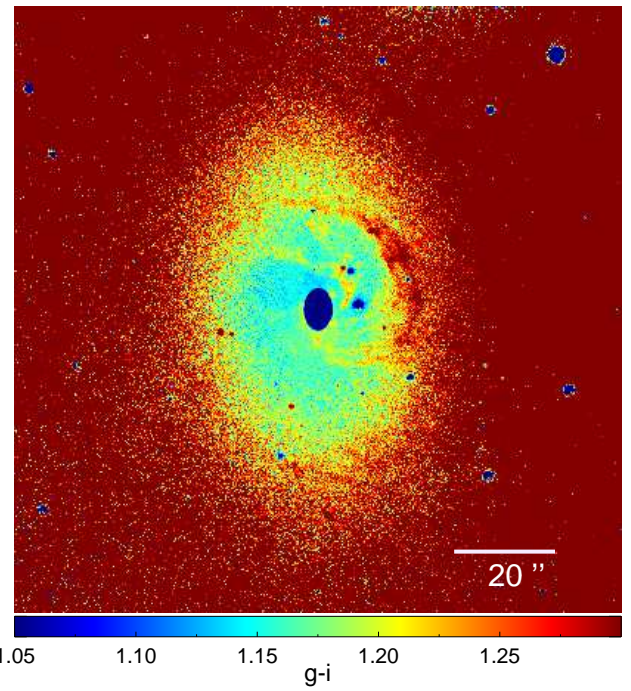
Fig. A.5. IC 4889 color map.

Appendix B: The surface brightness profiles

g and i surface brightness profiles are given for each galaxy as measured with iraf/ellipse. The indicated radii are the mean geometric radii of each fitted ellipse. Radii are given in arc seconds, while surface brightness, in mag/arcsec^2.
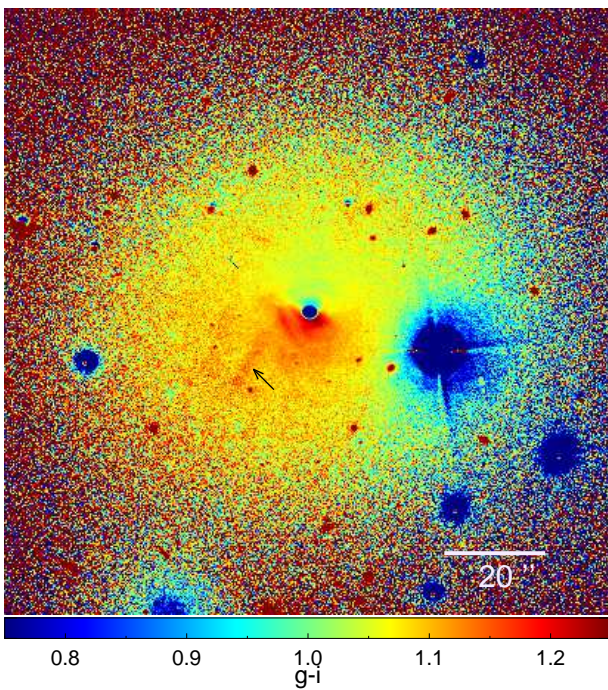
Fig. A.4. NGC 4240 color map.

Appendix A: The color maps

$g - i$ color maps are given for all five galaxies. Each panel has a different angular scale, appropriate to indicate relevant color features in each galaxy. For all figures North is up, East, to the left.
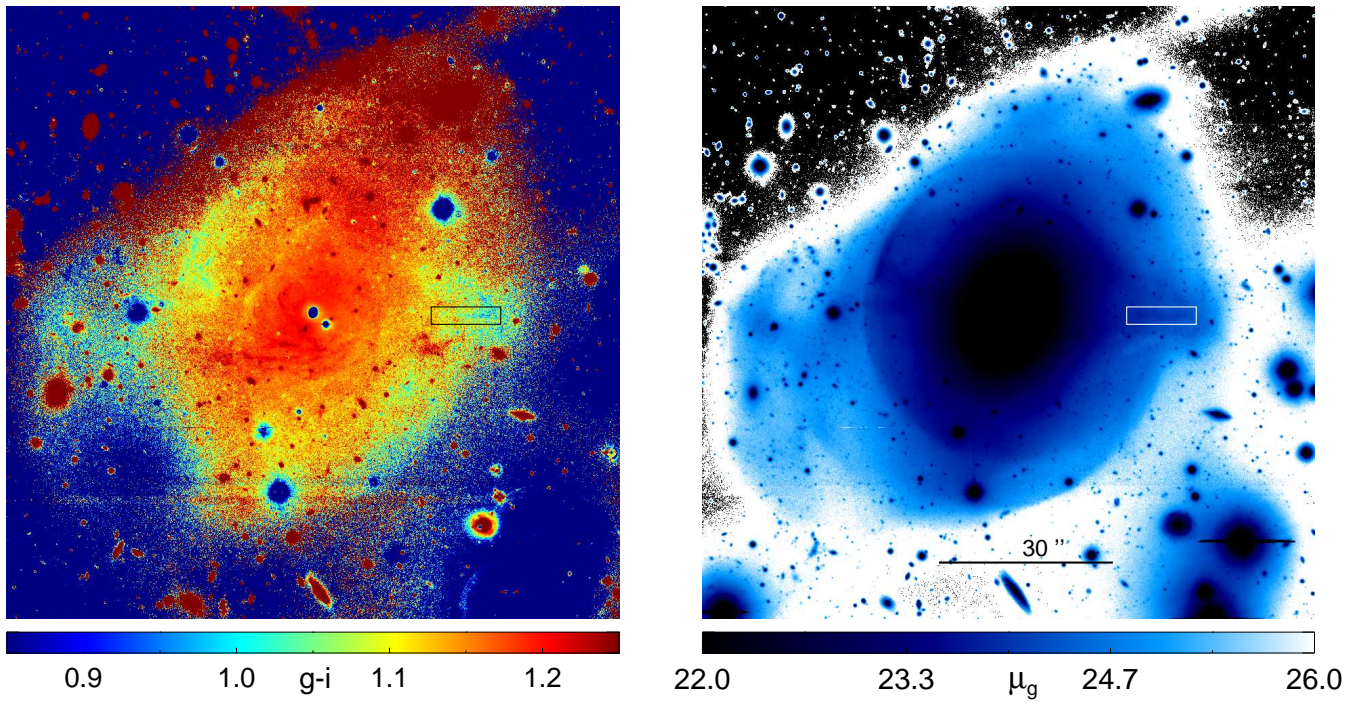
Fig. A.2. *Left panel*: $g - i$ color map of NGC 2865. *Right panel*: g surface brightness map of NGC 2865. Both figures share the same size and scale. The black/white box indicates the radial feature discussed in the text.

Fig. A.3. $g - i$ color map for the central parts of NGC 3962. *Left panel*: Gemini/GMOS map, $1'$ aside. The central blue area is due to detector saturation. *Right panel*: SOAR/SAM color map, $30''$ aside. Albeit with lower S/N, it shows details unseen in the Gemini image due to saturation.

Table B.1. NGC 2271 surface photometry

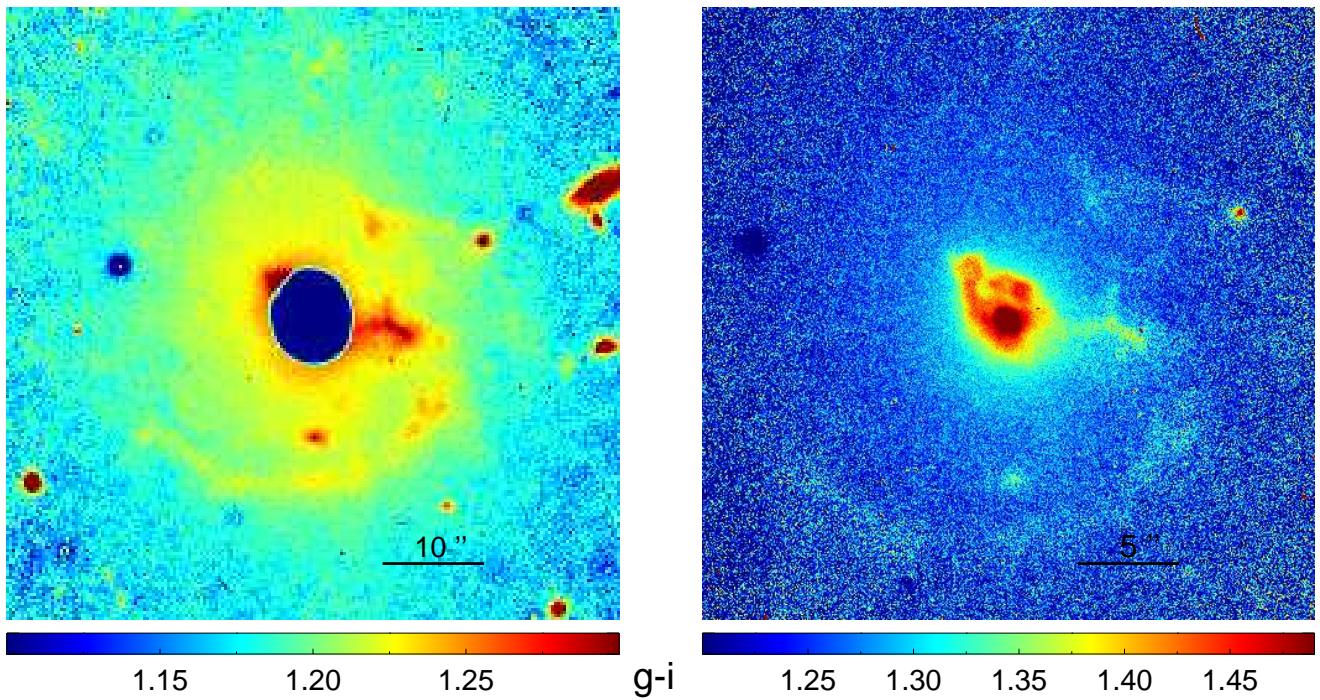| R	g	g_{err}	i	i_{err}
2.36	18.630	0.000	17.352	0.000
2.58	18.719	0.000	17.441	0.000
2.82	18.810	0.000	17.531	0.000
3.08	18.902	0.000	17.621	0.000
3.36	18.995	0.000	17.715	0.001
3.66	19.091	0.000	17.813	0.001
4.00	19.189	0.000	17.912	0.001
4.35	19.287	0.000	18.013	0.001
4.73	19.387	0.000	18.114	0.001
5.16	19.495	0.000	18.223	0.001
5.63	19.612	0.000	18.341	0.001
6.16	19.738	0.000	18.469	0.001
6.74	19.869	0.000	18.597	0.001
7.35	19.997	0.000	18.731	0.001
8.03	20.131	0.000	18.869	0.001
8.79	20.273	0.000	19.012	0.002
9.58	20.413	0.000	19.156	0.002
10.48	20.569	0.001	19.315	0.002
11.46	20.733	0.001	19.482	0.003
12.55	20.911	0.001	19.664	0.003
13.77	21.103	0.001	19.861	0.004
15.08	21.295	0.001	20.054	0.004
16.66	21.522	0.001	20.288	0.005
18.44	21.747	0.002	20.521	0.007
20.44	21.976	0.002	20.760	0.008
22.93	22.226	0.002	21.013	0.011
25.75	22.483	0.003	21.288	0.014
28.98	22.732	0.004	21.550	0.017
32.47	22.969	0.005	21.795	0.022
36.39	23.211	0.006	22.058	0.028
40.43	23.435	0.007	22.305	0.035
44.47	23.649	0.009	22.520	0.042
48.92	23.868	0.011	22.747	0.052
53.81	24.080	0.013	22.988	0.064
59.19	24.316	0.016	23.223	0.079
65.11	24.572	0.021	23.500	0.101
71.63	24.781	0.025	23.663	0.117
78.79	24.898	0.028	23.885	0.142
86.67	25.201	0.036	24.123	0.174
95.33	25.349	0.042	24.288	0.200
104.87	25.547	0.050	24.375	0.215
115.35	25.558	0.050	24.390	0.218

Table B.2. NGC 2865 surface photometry

R	g	g_{err}	i	i_{err}
3.65	18.557	0.000	17.547	0.000
3.99	18.681	0.000	17.665	0.000
4.37	18.808	0.000	17.784	0.000
4.77	18.938	0.000	17.906	0.000
5.22	19.073	0.000	18.038	0.000
5.72	19.210	0.000	18.172	0.000
6.20	19.340	0.000	18.305	0.000
6.77	19.476	0.000	18.444	0.000
7.40	19.621	0.000	18.581	0.000
8.09	19.764	0.000	18.727	0.000
8.85	19.905	0.000	18.871	0.000
9.65	20.039	0.001	19.001	0.000
10.53	20.168	0.001	19.136	0.000
11.56	20.308	0.001	19.274	0.001
12.68	20.458	0.001	19.424	0.001
14.02	20.633	0.001	19.594	0.001
15.52	20.819	0.001	19.785	0.001
17.17	21.011	0.001	19.987	0.001
18.95	21.212	0.002	20.189	0.001
21.00	21.428	0.002	20.410	0.001
23.19	21.648	0.002	20.632	0.002
25.91	21.888	0.003	20.874	0.002
28.99	22.126	0.004	21.121	0.003
31.63	22.310	0.004	21.310	0.003
34.64	22.519	0.005	21.522	0.004
38.28	22.767	0.006	21.762	0.005
42.17	22.987	0.008	21.983	0.006
46.38	23.164	0.009	22.175	0.007
51.02	23.363	0.011	22.378	0.009
56.12	23.554	0.013	22.583	0.011
61.73	23.758	0.016	22.793	0.013
67.91	24.007	0.020	23.026	0.016
74.70	24.300	0.026	23.333	0.021
82.17	24.616	0.034	23.671	0.029
90.39	25.054	0.051	24.099	0.043
99.42	25.436	0.072	24.586	0.067
109.37	25.627	0.086	24.885	0.087
120.30	25.880	0.107	25.081	0.104
132.33	26.171	0.140	25.564	0.159

Table B.3. NGC 3962 surface photometry

R	g	g_{err}	i	i_{err}
5.82	18.990	0.000	17.844	0.001
6.38	19.116	0.000	17.976	0.001
6.98	19.239	0.000	18.104	0.001
7.63	19.361	0.000	18.226	0.001
8.34	19.478	0.001	18.344	0.001
9.13	19.594	0.001	18.469	0.001
10.10	19.725	0.001	18.595	0.001
11.10	19.858	0.001	18.740	0.001
12.29	20.010	0.001	18.900	0.002
13.61	20.177	0.001	19.074	0.002
15.07	20.355	0.001	19.257	0.002
16.59	20.530	0.001	19.440	0.002
18.26	20.710	0.002	19.630	0.003
20.06	20.891	0.002	19.808	0.003
21.97	21.061	0.002	19.989	0.004
24.17	21.239	0.003	20.176	0.005
26.66	21.430	0.003	20.366	0.006
29.33	21.612	0.004	20.553	0.007
32.23	21.787	0.004	20.725	0.008
35.10	21.936	0.005	20.869	0.009
38.18	22.069	0.006	21.000	0.010
41.88	22.218	0.006	21.150	0.012
46.26	22.375	0.007	21.319	0.014
51.01	22.547	0.009	21.499	0.016
55.94	22.723	0.010	21.678	0.019
60.98	22.882	0.012	21.841	0.022
66.48	23.067	0.014	22.031	0.027
73.13	23.282	0.017	22.257	0.033
80.44	23.526	0.021	22.489	0.040
88.49	23.775	0.027	22.744	0.051
97.33	24.028	0.033	22.921	0.059
107.07	24.378	0.046	23.360	0.088
117.78	24.712	0.062	23.611	0.109
129.55	25.094	0.086	23.771	0.125
142.51	25.323	0.107	24.316	0.201
156.76	26.018	0.196	25.150	0.396
172.43	26.870	0.395	26.267	0.875

Table B.4. NGC 4240 surface photometry

R	g	g_{err}	i	i_{err}
1.23	17.672	0.000	17.039	0.000
1.34	17.780	0.000	17.042	0.000
1.47	17.915	0.000	17.045	0.000
1.61	18.051	0.000	17.075	0.000
1.76	18.183	0.000	17.180	0.000
1.92	18.313	0.000	17.305	0.000
2.09	18.438	0.000	17.427	0.000
2.26	18.554	0.000	17.542	0.000
2.44	18.664	0.000	17.650	0.000
2.63	18.766	0.000	17.753	0.000
2.84	18.863	0.000	17.858	0.000
3.08	18.971	0.000	17.972	0.000
3.35	19.091	0.000	18.102	0.000
3.71	19.235	0.000	18.256	0.000
4.21	19.417	0.000	18.449	0.000
4.90	19.631	0.000	18.656	0.000
5.54	19.835	0.000	18.852	0.000
6.15	20.006	0.000	19.031	0.000
6.79	20.170	0.000	19.202	0.000
7.53	20.343	0.000	19.380	0.000
8.32	20.515	0.000	19.555	0.000
9.13	20.689	0.000	19.732	0.000
10.02	20.893	0.000	19.937	0.000
11.03	21.117	0.000	20.167	0.000
12.16	21.344	0.000	20.399	0.000
13.32	21.546	0.000	20.603	0.000
14.62	21.736	0.000	20.798	0.000
16.04	21.917	0.000	20.985	0.001
17.58	22.092	0.000	21.174	0.001
19.19	22.243	0.001	21.311	0.001
20.99	22.415	0.001	21.523	0.001
23.13	22.602	0.001	21.688	0.001
25.34	22.780	0.001	21.880	0.001
27.97	22.996	0.001	22.091	0.001
30.94	23.256	0.001	22.384	0.002
33.94	23.521	0.002	22.650	0.002
37.39	23.813	0.002	22.960	0.003
41.13	24.108	0.003	23.220	0.004
45.50	24.411	0.004	23.618	0.006
50.50	24.732	0.005	23.930	0.008
55.89	25.041	0.007	24.277	0.011
61.95	25.388	0.009	24.630	0.015
69.30	25.777	0.013	24.969	0.021
74.52	26.024	0.017	25.146	0.025

Table B.5. IC 4889 surface photometry

R	g	g_{err}	i	i_{err}
2.57	17.980	0.000	17.319	0.000
2.83	18.092	0.000	17.319	0.000
3.12	18.203	0.000	17.319	0.000
3.41	18.324	0.000	17.320	0.000
3.74	18.453	0.000	17.372	0.000
4.11	18.581	0.000	17.502	0.000
4.52	18.716	0.000	17.635	0.000
4.98	18.849	0.000	17.768	0.000
5.46	18.980	0.000	17.904	0.001
6.00	19.123	0.000	18.042	0.001
6.67	19.298	0.000	18.209	0.001
7.28	19.428	0.000	18.338	0.001
8.03	19.574	0.000	18.482	0.001
8.75	19.699	0.000	18.677	0.001
9.65	19.837	0.000	18.830	0.001
10.64	20.009	0.000	18.930	0.001
11.70	20.160	0.000	19.075	0.001
12.79	20.303	0.001	19.216	0.002
13.96	20.444	0.001	19.354	0.002
15.27	20.594	0.001	19.502	0.002
16.78	20.764	0.001	19.651	0.003
18.32	20.927	0.001	19.812	0.003
19.91	21.083	0.001	19.967	0.003
21.75	21.247	0.001	20.135	0.004
23.87	21.437	0.002	20.316	0.005
26.52	21.664	0.002	20.508	0.006
29.27	21.891	0.002	20.718	0.007
32.38	22.132	0.003	20.932	0.008
36.16	22.403	0.004	21.168	0.010
40.36	22.687	0.005	21.411	0.013
44.99	22.965	0.006	21.638	0.016
50.01	23.222	0.008	21.845	0.019
55.68	23.493	0.010	22.005	0.022
61.74	23.748	0.013	22.235	0.027
68.51	24.027	0.017	22.463	0.033
79.26	24.486	0.025	22.616	0.038
88.12	24.755	0.032	22.798	0.045
97.77	25.153	0.046	23.011	0.054
110.10	25.633	0.071	23.285	0.069
122.16	26.178	0.115	23.613	0.093
139.19	27.188	0.269	23.959	0.126